

# Size and velocity-dispersion evolution of early-type galaxies in a $\Lambda$ cold dark matter universe

Carlo Nipoti<sup>1\*</sup>, Tommaso Treu<sup>2</sup>, Alexie Leauthaud<sup>3</sup>, Kevin Bundy<sup>3</sup>, Andrew B. Newman<sup>4</sup> and Matthew W. Auger<sup>5</sup>

<sup>1</sup>*Astronomy Department, University of Bologna, via Ranzani 1, I-40127 Bologna, Italy*

<sup>2</sup>*Department of Physics, University of California, Santa Barbara, CA 93106-9530, USA*

<sup>3</sup>*Institute for the Physics and Mathematics of the Universe (IPMU), The University of Tokyo, Chiba 277-8582, Japan*

<sup>4</sup>*Cahill Center for Astronomy & Astrophysics, California Institute of Technology, MS 249-17, Pasadena, CA 91125*

<sup>5</sup>*Institute of Astronomy, University of Cambridge, Madingley Road, Cambridge CB3 0HA*

Resubmitted, 3 February 2012

## ABSTRACT

Early-type galaxies (ETGs) are observed to be more compact at  $z \gtrsim 2$  than in the local universe. Remarkably, much of this size evolution appears to take place in a short  $\sim 1.8$  Gyr time span between  $z \sim 2.2$  and  $z \sim 1.3$ , which poses a serious challenge to hierarchical galaxy formation models where mergers occurring on a similar timescale are the main mechanism for galaxy growth. We compute the merger-driven redshift evolution of stellar mass  $M_* \propto (1+z)^{a_M}$ , half-mass radius  $R_e \propto (1+z)^{a_R}$  and velocity-dispersion  $\sigma_0 \propto (1+z)^{a_\sigma}$  predicted by concordance  $\Lambda$  Cold Dark Matter for a typical massive ETG in the redshift range  $z \sim 1.3 - 2.2$ . Neglecting dissipative processes, and thus maximizing evolution in surface density, we find  $-1.5 \lesssim a_M \lesssim -0.6$ ,  $-1.9 \lesssim a_R \lesssim -0.7$  and  $0.06 \lesssim a_\sigma \lesssim 0.22$ , under the assumption that the accreted satellites are spheroids. It follows that the predicted  $z \sim 2.2$  progenitors of  $z \sim 1.3$  ETGs are significantly less compact (on average a factor of  $\sim 2$  larger  $R_e$  at given  $M_*$ ) than the quiescent galaxies observed at  $z \gtrsim 2$ . Furthermore, we find that the scatter introduced in the size-mass correlation by the predicted merger-driven growth is difficult to reconcile with the tightness of the observed scaling law. We conclude that – barring unknown systematics or selection biases in the current measurements – minor and major mergers with spheroids are not sufficient to explain the observed size growth of ETGs within the standard model.

**Key words:** galaxies: elliptical and lenticular, cD — galaxies: formation — galaxies: kinematics and dynamics — galaxies: structure — galaxies: evolution

## 1 INTRODUCTION

Photometric and spectroscopic observations of high-redshift ( $z \gtrsim 2$ ) early-type galaxies (ETGs) suggest that these objects may be remarkably more compact (e.g. Stiavelli et al. 1999; Daddi et al. 2005; Trujillo et al. 2006; Zirm et al. 2007; Cimatti et al. 2008; van der Wel et al. 2008; van Dokkum et al. 2008; Saracco, Longhetti, & Andreon 2009; Cassata et al. 2011; Cimatti, Nipoti, & Cassata 2011; Damjanov et al. 2011; Saracco, Longhetti, & Gargiulo 2011) and have higher velocity dispersion (Cenarro & Trujillo 2009; Cappellari et al. 2009; van Dokkum, Kriek, & Franx 2009; van de Sande et al. 2011) than their local counterparts.

In the past few years, much theoretical work has been devoted to explaining the size evolution of massive ETGs

since  $z \gtrsim 2$ . Dissipative effects, such as star formation and gas accretion, are expected to go in the opposite direction and increase galaxy stellar density (Robertson et al. 2006; Ciotti, Lanzoni, & Volonteri 2007; Covington et al. 2011). Therefore attention has focused on dissipationless (“dry”) mergers, which appear to be the most promising mechanism to reproduce the observed evolutionary trends. Even though some groups have been able to reproduce the observed mean evolution by considering the combined effects of dry major and minor mergers, a potential contribution from active galactic nuclei (AGN; Fan et al. 2008, 2010; Ragone-Figueroa & Granato 2011), as well as a number of subtle observational issues (Hopkins et al. 2010a; Mancini et al. 2010; Oser et al. 2012), it is clear that the tension is far from resolved. Reproducing the average trend is only the first step. A successful model needs to also reproduce under the same assumption other properties of the mass-size/velocity dis-

\* E-mail: carlo.nipoti@unibo.it

persion correlations, including environmental dependencies (Cooper et al. 2012; Shankar et al. 2011) and their tightness (Nipoti, Treu, & Bolton 2009a, hereafter N09a; Nipoti et al. 2009b, hereafter N09b; Bernardi et al. 2011; Nair, van den Bergh, & Abraham 2011).

The results of Newman et al. (2010, hereafter N10) further raise the stakes of the theoretical challenge. Bridging the gap between the local universe and  $z \gtrsim 2$ , they found that ETGs at  $z \sim 1.3$  are only moderately smaller in size than present-day ETGs at fixed velocity dispersion. Together with results at higher redshifts, this suggests that ETGs have evolved at a very rapid pace between  $z \sim 2.2$  and  $z \sim 1.3$ , followed by more gentle evolution until the present day (see also Cimatti, Nipoti, & Cassata 2011; Raichoor et al. 2012; Newman et al. 2012, hereafter N12). These findings are confirmed and extended by the analysis of deep CANDELS images which show that the observed visible satellites cannot account for the evolution in size and number density of massive ETGs by minor merging (N12, see also Bluck et al. 2011).

Whereas most theoretical papers so far have focused on the entire evolutionary baseline  $z \gtrsim 2$  to the present, in this paper we focus on the shorter time span between  $z \sim 2.2$  and  $z \sim 1.3$ . This short timescale allows us to follow up a simple yet powerful and conservative approach. We start from two well-defined samples at  $z \sim 1.3$ , evolve them back in time to  $z \sim 2.2$  and compare them to observational samples at this higher redshift. In order to maximize the size evolution we neglect all dissipative processes, assuming that galaxies grow only by dry mergers. In other words, for given stellar-mass growth rate our models predict the maximum possible growth in size. Stellar mass could grow more than predicted by our models (as conversion of gas into stars is not accounted for), but, as mentioned above, this process is believed to have the effect of making galaxies more compact. In this sense our model is extreme: if it fails to reproduce the observed growth, then additional physical processes (e.g. feedback from AGN) or perhaps unknown selection effects must be considered in order to hope to reconcile the hierarchical model with the data. However, our dissipationless evolution model is also realistic in the sense that we adopt major and minor mergers rates and parameters taken from  $\Lambda$  Cold Dark Matter ( $\Lambda$ CDM) cosmological simulations. We then used detailed  $N$ -body simulations of individual mergers to compute the consequences of the mergers on galaxy structure and make robust predictions of their evolution in size, dark and luminous mass, and stellar velocity dispersion. For simplicity we limit ourselves to mergers between spheroidal systems. Our approach combines the benefits of detailed numerical simulations of individual merger events with the required knowledge of merging parameters that can only be gathered from large-volume cosmological simulations (for the dissipative case see Robertson et al. 2006; Hopkins et al. 2009). This paper supercedes our previous work (N09a; N09b) based on individual  $N$ -body simulations in idealized merging conditions.

Our reference data consist of two well-defined samples of ETGs: the first sample consists of galaxies with measured stellar velocity dispersion, size, and stellar mass. The second sample consists of galaxies with measured size and stellar mass, but not necessarily velocity dispersion. The first sample is in principle cleaner to interpret, since stellar ve-

locity dispersion is changed relatively little by dry mergers (Hausman & Ostriker 1978; Hernquist, Spiegel, & Heyl 1993; Nipoti, Londrillo, & Ciotti 2003; Naab, Johansson, & Ostriker 2009) and therefore provides an excellent “label” to match samples at different redshifts. At the moment, there are only a handful of measurements of velocity dispersion at  $z \gtrsim 1.8$ . Hence, the statistical power of this diagnostic is currently limited. However, these calculations provide a useful benchmark and framework for interpreting the larger samples that are expected to be collected in the near future using multiplexed infrared spectrographs on large telescopes. The second sample is an order of magnitude larger in size, and currently provides the most stringent test of the galaxy-evolution models presented here.

The manuscript is organized as follows. In Section 2 we summarize the properties of our comparison samples. In Section 3 we describe our models based on three ingredients: i) mergers and mass accretion rates inferred from cosmological numerical simulations; ii) simple recipes to connect halo and stellar mass based on abundance matching techniques; iii) prescriptions for evolution of velocity dispersion and size based on individual merger  $N$ -body simulations. As it turns out, the major source of theoretical uncertainty is related to the second step, i.e. matching stellar with halo mass. To quantify this uncertainty, we consider three independent recipes and we show that our conclusions are robust with respect to this choice. In Section 4 we compare our numerical predictions to the data. In Section 5 we perform a consistency check of our models by comparing the descendants of the  $z \sim 1.3$  samples with the local scaling relations. The results are discussed in Section 6, and in Section 7 we draw our conclusions.

Throughout the paper we assume  $H_0 = 73 \text{ km s}^{-1} \text{ Mpc}^{-1}$ ,  $\Omega_\Lambda = 0.75$  and  $\Omega_m = 0.25$ , consistent with the values adopted in the Millenium I and II simulations (Springel et al. 2005; Boylan-Kolchin et al. 2009). We also adopt a Chabrier (2003) initial mass function (IMF). When necessary we transform published values of stellar mass to a Chabrier IMF, using appropriate renormalization factors. We note that our results are independent of the specific choice of the IMF, provided that the same IMF is used consistently to estimate stellar masses of observed galaxies and to connect observed properties with dark matter halos.

## 2 OBSERVATIONAL DATA

### 2.1 Early-type galaxies at $z \sim 1.3$

Our first reference sample at  $z \sim 1.3$  is comprised of spheroidal galaxies in the redshift interval  $1 < z < 1.6$  observed by N10. Following N10 we consider only the sub-sample of galaxies with central stellar velocity dispersion  $\sigma_0 > 200 \text{ km s}^{-1}$ , which is estimated to be complete at the 90% level. This sample (hereafter V1; see Table 1) consists of 13 ETGs with stellar mass in the range  $10.5 \lesssim \log M_*/M_\odot \lesssim 11.3$ , with average redshift  $\langle z \rangle \simeq 1.3$ .

Our second reference sample, without stellar velocity dispersion measures, consists of quiescent ETGs in the redshift range  $1 < z < 1.6$  ( $\langle z \rangle \simeq 1.3$ ) selected from the sample of N12. This sample (hereafter R1, see Table 1) comprises

**Table 1.** Properties of the samples of observed galaxies.

Sample	Range of $z$	$\langle z \rangle$	$N_{\text{gal}}$	$\sigma_0$	References
V1	$1 < z < 1.6$	1.3	13	yes	1
R1	$1 < z < 1.6$	1.3	150	no	2
V2	$1.8 < z < 2.2$	1.9	4	yes	3, 4, 5, 6
R2	$2 < z < 2.6$	2.2	53	no	2, 4, 7, 8

$N_{\text{gal}}$ : number of galaxies.  $\sigma_0=\text{yes}(\text{no})$ : measures of  $\sigma_0$  are (are not) available. References: 1=N10, 2=N12, 3= Cappellari et al. (2009), 4=van Dokkum, Kriek, & Franx (2009), 5=Onodera et al. (2010), 6=van de Sande et al. (2011), 7=van Dokkum et al. (2008), 8=Kriek et al. (2008).

150 galaxies with measures of  $R_e$  and stellar mass complete above  $M_* > 10^{10.4} M_\odot$ .

## 2.2 Early-type galaxies at $z \sim 2.2$

At  $z \gtrsim 1.8$ , there are only a handful of ETGs with measured stellar velocity dispersion. Thus our first comparison sample (hereafter V2, see Table 1) consists of 4 galaxies taken from the studies of Cappellari et al. (2009), van Dokkum, Kriek, & Franx (2009), Onodera et al. (2010, upper limit on  $\sigma_0$ ) and van de Sande et al. (2011). The average redshift of sample V2 is  $\langle z \rangle \simeq 1.9$ . Substantially larger is our second comparison sample, comprised of ETGs in the redshift range  $2 < z < 2.6$  with measured stellar mass and effective radius. We construct this sample (hereafter R2, see Table 1) by selecting quiescent galaxies with  $M_* > 10^{10.4} M_\odot$  from the studies by van Dokkum et al. (2008), Kriek et al. (2008), van Dokkum, Kriek, & Franx (2009) and N12. This results in a sample of 53 ETGs with properties very similar to those of our sample of ETGs at  $z \sim 1.3$ , well-suited for a detailed comparison. Note that we use the term ETGs in a broad sense, including both morphologically selected spheroids and quiescent galaxies. The average redshift of sample R2 is  $\langle z \rangle \simeq 2.2$ , which we adopt as reference redshift when comparing models with observations.

## 3 MODELS

In this Section we describe how we compute the predicted properties of higher- $z$  progenitors of our samples of galaxies at  $z \sim 1.3$ . For each galaxy, we need to compute evolution in stellar mass, effective radius, and stellar velocity dispersion, driven by the evolution of its dark matter (DM) halo mass  $M_h$  as predicted by cosmological  $N$ -body simulations.

The growth of stellar mass  $M_*$  with  $z$  can be written in terms of  $dM_h/dz$  as

$$\frac{dM_*}{dz} = \frac{dM_*}{dM_h} \frac{dM_h}{dz}. \quad (1)$$

In turn, the evolution of the central stellar velocity dispersion  $\sigma_0$  is given by

$$\frac{d\sigma_0}{dz} = \frac{d\sigma_0}{dM_*} \frac{dM_*}{dz} = \frac{d\sigma_0}{dM_*} \frac{dM_*}{dM_h} \frac{dM_h}{dz}, \quad (2)$$

while the evolution of the effective radius  $R_e$  is given by

$$\frac{dR_e}{dz} = \frac{dR_e}{dM_*} \frac{dM_*}{dz} = \frac{dR_e}{dM_*} \frac{dM_*}{dM_h} \frac{dM_h}{dz}. \quad (3)$$

Therefore, the key ingredients of our model are the four derivatives  $dM_h/dz$ ,  $dM_*/dM_h$ ,  $d\sigma_0/dM_*$  and  $dR_e/dM_*$ . Sections 3.1 to 3.3 describe in detail how these derivatives are calculated based on up-to-date cosmological  $N$ -body simulations, abundance matching results, and detailed simulations of individual merger events. Section 3.4 combines all the ingredients to compute the evolution of individual galaxies.

### 3.1 Halo mass growth rate ( $dM_h/dz$ )

#### 3.1.1 Total mass growth rate

Based on the Millenium I and II simulations, Fakhouri, Ma, & Boylan-Kolchin (2010) estimate the halo mass growth rate as follows. The average mass variation with redshift of a DM halo of mass  $M_h$  is

$$\frac{d \ln M_h}{dz} = - \frac{\dot{M}_0}{10^{12} M_\odot H_0} \frac{1 + az}{1 + z} \left( \frac{M_h}{10^{12} M_\odot} \right)^{b-1}, \quad (4)$$

with  $\dot{M}_0 = 46.1 M_\odot/\text{yr}$ ,  $a = 1.11$  and  $b = 1.1$ . By integrating equation (4) between  $z_d$  (the redshift of the descendant halo) and  $z$  we obtain

$$\left[ \frac{M_h(z)}{10^{12} M_\odot} \right]^{1-b} = \left[ \frac{M_h(z_d)}{10^{12} M_\odot} \right]^{1-b} - \frac{1-b}{H_0} \frac{\dot{M}_0}{10^{12} M_\odot} I_{z_d}(z), \quad (5)$$

where

$$I_{z_d}(z) \equiv \int_{z_d}^z \frac{1 + az'}{1 + z'} dz' = \left[ a(z - z_d) - (a - 1) \ln \frac{1 + z}{1 + z_d} \right]. \quad (6)$$

This formalism can be used to quantify the growth rate of the halo of our descendant galaxies. The total accreted DM fraction  $\delta M_h(z)/M_h(z_d)$  is shown in Fig. 1 for a representative descendant halo at  $z_d = 1.3$  with  $M_h(z_d) = 5 \times 10^{12} M_\odot$ . Note that the estimate of Fakhouri, Ma, & Boylan-Kolchin (2010) is appropriate for main halos, not for sub-halos. However, the large majority ( $\sim 80\%$ ) of massive ( $M_* \sim 10^{11} M_\odot$ ) red galaxies are central galaxies of halos (van den Bosch et al. 2008) even in the local universe. Therefore, we can simplify our treatment by assuming that our samples of massive ETGs consist of central halo galaxies (see also van der Wel et al. 2009).

#### 3.1.2 Mass growth rate due to mergers only

The total growth rate shown in Figure 1 includes the contribution of mergers with other halos as well as accretion of diffuse DM (Fakhouri & Ma 2010; Genel et al. 2010). For our purposes, it is important to distinguish the two contributions, because—as discussed below—we expect no substantial growth in stellar mass associated with diffuse accretion of DM<sup>1</sup>.

The merger rate is expected to depend on the mass of the main halo  $M_h$ , on the redshift  $z$ , on the mass ratio  $\xi$  between the satellite and the main halo, and on the merger

<sup>1</sup> Of course it is possible that the so-called “cold-flow” accretion of baryons is important in galaxy evolution (e.g. Kereš et al. 2005), but this is expected to be accretion of gaseous baryons, which we can neglect in our pure dry-merger model.

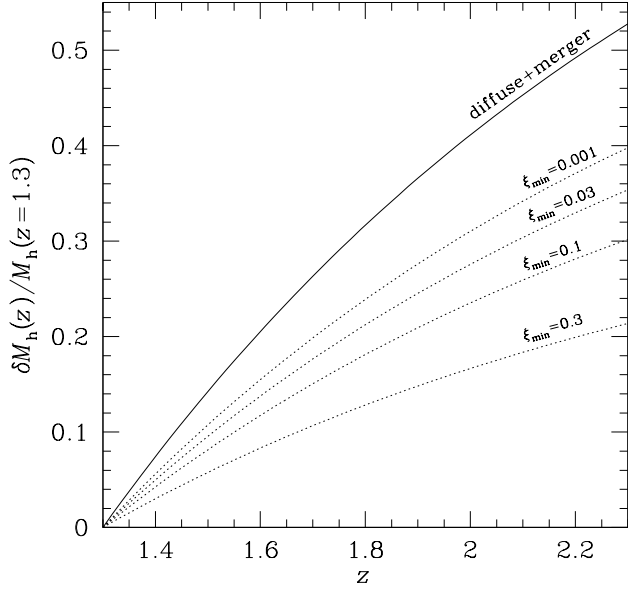


**Figure 1.** The solid curve represents the total fraction of DM mass accreted between  $z$  and  $z_d = 1.3$  of a descendant halo with mass  $M_h(z_d) = 5 \times 10^{12} M_\odot$  at  $z_d = 1.3$  as a result of mergers and diffuse accretion:  $\delta M_h(z) = M_h(z_d) - M_h(z)$ . The dotted lines represent the fraction of DM mass accreted between  $z$  and  $z_d = 1.3$ , as a result of mergers only with mass-ratio  $\xi \geq \xi_{\min}$ . The curves are based on the analysis of the Millenium I and II simulations by Fakhouri, Ma, & Boylan-Kolchin (2010).

orbital parameters (e.g., orbital energy  $E$  and orbital angular momentum  $L$ ). Omitting for simplicity the explicit dependence on  $E$  and  $L$ , the halo evolution due to mergers can be written as

$$\left[ \frac{d^2 M_h}{dz d\xi} \right]_{\text{merg}}(M_h, \xi, z) = \xi M_h \frac{d^2 N_{\text{merg}}}{dz d\xi}(M_h, \xi, z), \quad (7)$$

where  $\xi \leq 1$  is the mass ratio of the two DM halos involved in the merger, and  $d^2 N_{\text{merg}}/dz d\xi$  is the distribution in  $z$  and  $\xi$  of the number of mergers per halo. The mass accretion rate due to mergers with mass ratio higher than  $\xi_{\min}$  is therefore given by

$$\left[ \frac{dM_h}{dz} \right]_{\text{merg}} = - \int_{\xi_{\min}}^1 M_h(z) \xi \frac{d^2 N_{\text{merg}}}{dz d\xi} d\xi. \quad (8)$$

Based on the Millenium I and II simulations, Fakhouri, Ma, & Boylan-Kolchin (2010) estimate

$$\frac{d^2 N_{\text{merg}}}{d\xi dz}(M, \xi, z) = A \left( \frac{M_h}{10^{12} M_\odot} \right)^\alpha \xi^\beta \exp \left[ \left( \frac{\xi}{z} \right)^\gamma \right] (1+z)^{\eta'}, \quad (9)$$

implying

$$\left[ \frac{dM_h}{10^{12} M_\odot} \right]_{\text{merg}} = -A I_{\xi_{\min}} \left[ \frac{M_h(z)}{10^{12} M_\odot} \right]^{\alpha+1} (1+z)^{\eta'} dz, \quad (10)$$

where

$$I_{\xi_{\min}} \equiv \int_{\xi_{\min}}^1 \xi^{\beta+1} \exp \left( \frac{\xi}{z} \right)^\gamma d\xi. \quad (11)$$

Following Fakhouri, Ma, & Boylan-Kolchin (2010), we assume  $A = 0.0104$ ,  $\xi = 9.72 \times 10^{-3}$ ,  $\alpha = 0.133$ ,  $\beta = -1.995$ ,

$\gamma = 0.263$  and  $\eta' = 0.0993$ . By integrating equation (10) we get

$$\frac{[\delta M_h]_{\text{merg}}(z)}{10^{12} M_\odot} = A I_{\xi_{\min}} \int_{z_d}^z \left[ \frac{M_h(z')}{10^{12} M_\odot} \right]^{\alpha+1} (1+z')^{\eta'} dz', \quad (12)$$

which is the DM mass accreted between  $z$  and  $z_d$  via mergers with mass ratio  $\xi \geq \xi_{\min}$ . This quantity, normalized to the total DM mass of the halo at  $z = z_d$ , is plotted in Fig. 1 for a representative halo of mass  $M_h = 5 \times 10^{12} M_\odot$  at redshift  $z_d = 1.3$ , for a range of values of  $\xi_{\min}$ . The plot shows that the most massive  $z \simeq 2.2$  progenitor of a typical  $z = 1.3$  halo is roughly half as massive as the descendant. However, only  $\sim 1/3$  of the mass of the descendant has been acquired via mergers (defined as  $\xi \geq 0.04$ ; Fakhouri & Ma 2010). The rest is acquired by diffuse accretion.

We note that the Millenium simulations, which we use to quantify merger rates, adopt a normalization of the mass variance  $\sigma_8 = 0.9$ , while the latest (seven-year) analysis of the Wilkinson Microwave Anisotropy Probe experiment (WMAP7) favours  $\sigma_8 \simeq 0.8$  (Komatsu et al. 2011). Though rescaling the numerical results to a different cosmology is not trivial (Angulo & White 2010), according to the analytic approach of Lacey & Cole (1993) the merger rates for  $\sigma_8 \simeq 0.8$  can be at most  $\sim 10\%$  higher than for the Millenium choice. Changing the merger rates by this amount would not alter any of our conclusions. Detailed estimates of the merger rates in a WMAP7 Universe will be available in the near future from the analysis of recent  $N$ -body simulations with updated cosmology (such as the Bolshoi Simulation; Klypin, Trujillo-Gomez, & Primack 2011).

### 3.1.3 Minimum merger mass-ratio $\xi_{\min}$

Not all DM accretion events contribute to the stellar-mass growth. In particular, very minor mergers are not expected to contribute significantly, because (i) their merging time can be extremely long (longer than the Hubble time) and (ii) only a very small fraction of their mass is in stars. For these reasons, only mergers with mass ratio larger than a critical value  $\xi_{\min}$  will be relevant to the growth of the stellar component of the galaxy.

The critical value of the satellite-main halo mass ratio  $\xi_{\min}$  can be identified on the basis of the merging timescales (see Hopkins et al. 2010b and references therein). Here we adopt the results of Boylan-Kolchin, Ma, & Quataert (2008), who, based on  $N$ -body simulations, estimated the relationship between merging time  $t_{\text{merg}}$  of a satellite and dynamical time  $t_{\text{dyn}}$  of the host halo. Boylan-Kolchin, Ma, & Quataert (2008) parametrize the orbits of the infalling satellites using circularity  $\eta = \sqrt{1 - e^2}$  (where  $e$  is the eccentricity) and  $r_{\text{circ}}(E)/r_{\text{vir}}$ , the radius of a circular orbit with the same energy  $E$  as the actual orbit (orbits characterized by larger values of  $r_{\text{circ}}(E)/r_{\text{vir}}$  are less bound). The merging timescale  $t_{\text{merg}}$  as a function of mass ratio  $\xi$ , is then given by

$$\frac{t_{\text{merg}}}{t_{\text{dyn}}} = \frac{a'}{\xi^{b'} \ln \left( 1 + \frac{1}{\xi} \right)} \exp(c'\eta) \left[ \frac{r_{\text{circ}}(E)}{r_{\text{vir}}} \right]^{d'}, \quad (13)$$

with  $a' = 0.216$ ,  $b' = 1.3$ ,  $c' = 1.9$  and  $d' = 1.0$  (Boylan-Kolchin, Ma, & Quataert 2008). Equation (13) has been estimated for bound orbits (with orbit parameters measured at

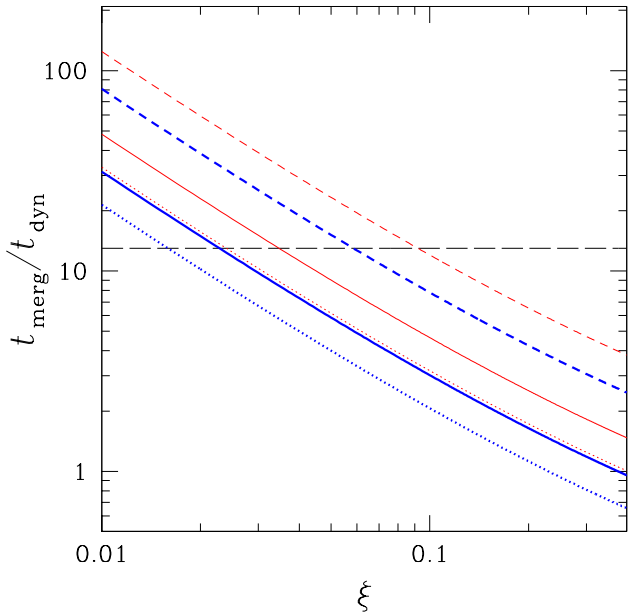


**Figure 2.** Merging time (in units of the main-halo dynamical time) as a function of the satellite-main halo mass ratio  $\xi$  for  $r_{\text{circ}}(E)/r_{\text{vir}} = 1$  (thin red) and  $r_{\text{circ}}(E)/r_{\text{vir}} = 0.65$  (thick blue), for different values of the circularity  $\eta = 0.3$  (dotted),  $\eta = 0.5$  (solid) and  $\eta = 1$  (dashed; Boylan-Kolchin, Ma, & Quataert 2008). Only accretion events with merging time below the horizontal long-dashed line can contribute to the growth of the stellar mass of the central galaxy in the redshift range 1.3 – 2.2.

$r_{\text{vir}}$ ), with  $\xi$  in the range  $0.025 \lesssim \xi \lesssim 0.3$ . The halo dynamical time  $t_{\text{dyn}}$  is defined as

$$t_{\text{dyn}} \equiv \left( \frac{r_{\text{vir}}^3}{GM_{\text{h}}} \right)^{1/2}, \quad (14)$$

where  $r_{\text{vir}}$  is the virial radius and  $M_{\text{h}}$  the mass of the main halo. It follows that  $t_{\text{dyn}} = (2/\Delta)^{1/2} H^{-1}$ , because, by definition,  $r_{\text{vir}}^3 = 2GM_{\text{h}}/\Delta H^2$ , where  $H(z)$  is the Hubble parameter at redshift  $z$ . So, for  $\Delta = 200$ ,  $t_{\text{dyn}} = 0.1H^{-1}$  independent of mass (Boylan-Kolchin, Ma, & Quataert 2008).

As a result, the time lag  $t_{\text{merg}}$  between the time when the satellites enters the virial radius of the halo, and the moment when the satellites is accreted by the central galaxy depends on  $\xi$  and  $z$ , but is independent of the halo mass. In this analysis, given the limited redshift interval, we can safely adopt a fixed value of  $\xi_{\text{min}}$ . The smallest value of  $t_{\text{H}} \equiv H(z)^{-1}$  in the redshift range  $z = 1.3 - 2.2$  is  $t_{\text{H,min}} = t_{\text{H}}(z = 2.2) \simeq 1.4 \text{ Gyr}$ . The cosmic time between  $z = 2.2$  and  $z = 1.3$  is  $\simeq 1.8 \text{ Gyr} \sim 1.3t_{\text{H,min}}$ . Therefore, we assume that only mergers with  $t_{\text{merg}} \lesssim 13t_{\text{dyn}}$  (i.e.  $t_{\text{merg}} \lesssim 1.3t_{\text{H}}(z)$ ) can contribute to the growth of the stellar component of the galaxy. *Note that this approach is conservative, since our merging criterion  $t_{\text{merg}} \lesssim 1.3t_{\text{H}}(z)$  gives an upper limit to the mass accreted via mergers by the descendant galaxy.*

In Fig. 2 we plot  $t_{\text{merg}}/t_{\text{dyn}}$  as a function of  $\xi$  for different combinations of the values of the parameters  $\eta$  and  $r_{\text{circ}}(E)$ , spanning the entire range explored by Boylan-Kolchin, Ma, & Quataert (2008):  $r_{\text{circ}}(E)/r_{\text{vir}} = 0.65, 1$  and  $\eta = 0.3, 0.5, 1$ . The critical ratio  $\xi_{\text{min}}$  (defined such that  $t_{\text{merg}} = 13t_{\text{dyn}} = 1.3t_{\text{H}}$ ) is in the range  $0.02 \lesssim \xi_{\text{min}} \lesssim 0.09$ .

We can refine our estimate of  $\xi_{\text{min}}$  based on the distribution of orbital parameters of infalling DM satellites in cosmological  $N$ -body simulations (Benson 2005; Wang et al. 2005; Zentner et al. 2005; Khochfar & Burkert 2006; Wetzel 2011). Although the details may vary from one study to another, the general consensus is that orbits are typically close to parabolic ( $E \sim 0$ ) and relatively eccentric (with typical circularity  $\eta \sim 0.5$  for bound orbits; Benson 2005; Zentner et al. 2005; Khochfar & Burkert 2006). Thus, taking as reference  $r_{\text{circ}}(E)/r_{\text{vir}} = 1$  (the least bound orbits among those explored by Boylan-Kolchin, Ma, & Quataert 2008) and  $\eta = 0.5$  we obtain  $\xi_{\text{min}} \sim 0.03$ , which we adopt as our fiducial minimum mass ratio. Interestingly, this value is close to that adopted by Fakhouri & Ma (2010) ( $\xi = 0.04$ ) to separate diffuse accretion and mergers. Therefore, in the terminology of Fakhouri & Ma (2010) we conclude that only mergers (and not diffuse accretion) contribute to the growth of the stellar component of a central galaxy of a halo, in the redshift interval considered here.

As anticipated above, an additional and independent argument to exclude very minor mergers is that sufficiently low-mass halos are expected to be star-poor (e.g. van den Bosch et al. 2007; Behroozi, Conroy, & Wechsler 2010, hereafter B10). Of course, these low-mass halos can contain significant amounts of gas, from which stars can form. However, we can neglect this effect in our pure dry-merging evolution scenario. Following van der Wel et al. (2009), we account for the fact that low-mass halos are star-poor by assuming that merging halos with mass  $M_{\text{h}} \lesssim 10^{11} M_{\odot}$  do not increase the stellar mass of the galaxy. The halos hosting our galaxies typically have  $\log M_{\text{h}}/M_{\odot} \sim 12.5 - 13$  at  $z \sim 1.3$ . For these halos the limit corresponds to  $\xi_{\text{min}} \sim 0.01 - 0.03$ , i.e. slightly less stringent than the value  $\xi_{\text{min}} \sim 0.03$  obtained from dynamical considerations. Therefore, we can safely adopt  $\xi_{\text{min}} = 0.03$  as our fiducial value, encompassing both dynamical and star formation efficiency limits.

To conclude this section we can use the formalism introduced above to compute the mass-weighted merger mass ratio

$$\langle \xi \rangle_M \equiv \frac{\int_{\xi_{\text{min}}}^1 \xi F_M d\xi}{\int_{\xi_{\text{min}}}^1 F_M d\xi}, \quad (15)$$

where  $F_M \equiv [d^2 M_{\text{h}}/dzd\xi]_{\text{merg}}(M_{\text{h}}, \xi, z)$ , and the number-weighted merger mass ratio

$$\langle \xi \rangle_N \equiv \frac{\int_{\xi_{\text{min}}}^1 \xi F_N d\xi}{\int_{\xi_{\text{min}}}^1 F_N d\xi} \quad (16)$$

where  $F_N \equiv d^2 N_{\text{merg}}/dzd\xi(M_{\text{h}}, \xi, z)$ . In our model  $\langle \xi \rangle_M$  and  $\langle \xi \rangle_N$  are independent of halo mass and redshift (see equations 7 and 9), and only weakly dependent on  $\xi_{\text{min}}$ . For  $\xi_{\text{min}} = 0.03$  we get  $\langle \xi \rangle_M \simeq 0.45$  and  $\langle \xi \rangle_N \simeq 0.21$ . In other words, if we wanted to describe the halo merging history simply with a single number, we could say that even though most mergers have typical mass ratios  $\xi \sim 0.2$ , most of the mass is accreted in higher mass-ratio mergers, typically with  $\xi \sim 0.45$ .

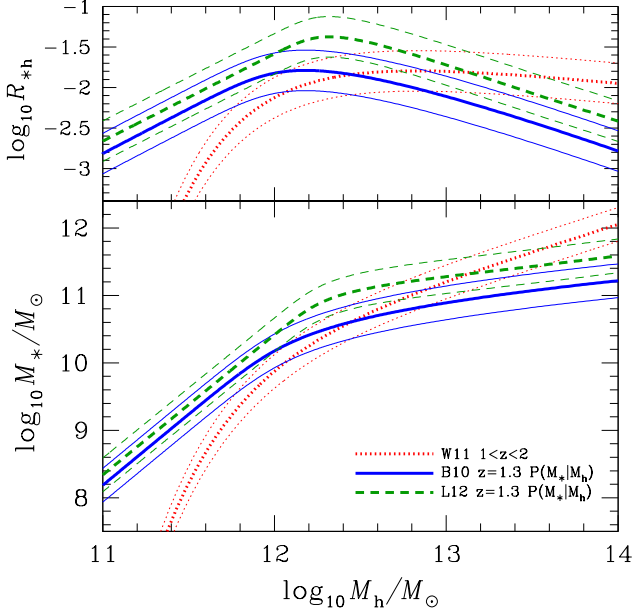


**Figure 3.** Stellar to DM mass ratio  $\mathcal{R}_{*h}$  (upper panel) and stellar mass  $M_*$  (lower panel) as functions of halo mass  $M_h$  according to prescriptions (i) (W11, thick dotted lines), (ii) (B10, thick solid lines) and (iii) (L12, thick dashed lines) for  $dM_*/dM_h$ . The corresponding thin lines show the estimated systematic uncertainty. In prescriptions (ii) and (iii) the SHMR depends on  $z$ . We plot here the fits for  $z = 1.3$  based on  $P(M_*|M_h)$ , as described in Section 3.2.1.

### 3.2 Stellar-to-halo mass relation ( $dM_*/dM_h$ )

#### 3.2.1 Assigning stellar mass to halos: $M_*(M_h)$

In general, the relationship between galaxy stellar mass and host halo mass depends on both the star formation history and the merger history (see B10; Guo et al. 2010). In a dry-merger scenario, when a halo of mass  $M_h$  undergoes a merger with mass ratio  $\xi$  the increase in DM mass is  $\xi M_h$ , and the increase in stellar mass is  $\mathcal{R}_{*h}\xi M_h$ , where  $\mathcal{R}_{*h}$  is the ratio of stellar to DM mass of the satellite. As  $\mathcal{R}_{*h}$  is expected to depend both on satellite mass  $\xi M_h$  and on redshift, in general we have

$$\frac{dM_*}{dM_h} = \frac{dM_*}{dM_h}(\xi, M_h, z) = \mathcal{R}_{*h}(\xi M_h, z). \quad (17)$$

At the time of this writing the stellar-to-halo mass relation (SHMR) is uncertain, mainly as a result of corresponding uncertainties in stellar mass measurements, and, at higher redshifts, of the lack of robust galaxy samples. The total *systematic* uncertainty in  $\log M_*$  (at fixed  $M_h$ ) is approximately  $\sim 0.25$  at  $z \lesssim 1$ , and possibly larger at higher redshift (B10). Several SHMRs are available in the literature, providing the relation between  $M_*$  and  $M_h$  as a function of redshift. Differences between these models can be generally accounted for by the systematics mentioned above. As we will show in the rest of the paper, this is the main source of uncertainty in our evolutionary models. We will thus consider three recent estimates of the SHMR and investigate how they affect our conclusions. The three prescriptions described in more detail below are based on the measurements by: (i) Wake et al. (2011, hereafter W11); (ii) B10; (iii) L12. Our study

will show that our conclusions are robust with respect to the choice of the prescription.

*Prescription (i)* In the framework of halo occupation distribution models, W11 find that in the redshift range  $1 < z < 2$  the dark-to-stellar mass ratio does not depend significantly on redshift. According to the best-fitting relation of W11, the median stellar mass  $M_*$  of the central galaxy of a halo of mass  $M_h$  is given by

$$M_* = \Theta(M_h)M_h, \quad (18)$$

where

$$\Theta(M_h) = \left[ \frac{M_t}{A_M} \left( \frac{M_h}{M_t} \right)^{1-\alpha_M} \exp \left( \frac{M_t}{M_h} - 1 \right) \right]^{-1}, \quad (19)$$

with  $A_M = 1.55 \times 10^{10} M_\odot$ ,  $\alpha_M = 0.8$  and  $M_t = 0.98 \times 10^{12} h^{-1} M_\odot$  (D. Wake, private communication<sup>2</sup>). In Fig. 3 we plot  $M_*$  and  $\mathcal{R}_{*h} \equiv M_*/M_h$  as functions of  $M_h$  according to this prescription together with the systematic uncertainty (0.25 dex in  $M_*$  at given  $M_h$ ). In summary, in this case we assume  $\mathcal{R}_{*h}(M, z) = \Theta(M)$ , independent of  $z$ . This first prescription is a useful benchmark in our analysis, because the interpretation of the halo and stellar mass evolution is straightforward when the SHMR is independent of  $z$ . However, there are reasons to think that the SHMR actually depends on  $z$  also at these redshifts. In fact, we note an important caveat with the Wake et al. SHMR: their halo occupation distribution model of the clustering data makes the implicit assumption that the SHMR is a power-law relation (see discussion in section 3.2 of Leauthaud et al. 2011a). This is problematic in light of accumulating evidence that the SHMR is not well described by a single power-law relation, especially at high stellar masses where it steepens considerably. For this reason, we expect a 10-40% difference between the  $M_{\min}$  values reported by W11 and the true mean halo mass (with larger errors for  $\sigma_{\log M_*} > 0.25$ , where  $\sigma_{\log M_*}$  is the scatter in  $\log M_*$  at given  $M_h$ , due to *statistical* errors). An example of the difference expected between  $M_{\min}$  and the true mean halo mass is shown in Leauthaud et al. (2011a, see their figure 3).

*Prescription (ii)* B10 provide fits to the SHMR as a function of both halo mass and redshift, in the range  $0 \lesssim z \lesssim 4$ . We take the correlation between halo mass  $M_h$  and stellar mass  $M_*$  as given in B10 (their equations 21, 22 and 25, and columns labelled “Free( $\mu, \kappa$ )” in their Table 2) to define  $\mathcal{R}_{*h}(M_h, z) \equiv M_*/M_h$ . The B10 fit for  $z = 1.3$  is shown in Fig. 3 with the associated systematic uncertainty (0.25 dex in  $M_*$  at given  $M_h$ ).

*Prescription (iii)* Recently Leauthaud et al. (2012, hereafter L12) have studied in great detail the SHMR as a function of halo mass and redshift at  $z \lesssim 1$ . To obtain a third independent estimate of the SHMR at high redshift we extrapolate the SHMR of L12 at  $z \gtrsim 1$ . In this case, we define  $\mathcal{R}_{*h}(M_h, z) \equiv M_*/M_h$ , where the correlation between  $M_h$  and  $M_*$  is given by the same fitting formula as in B10 (their equations 21, 22 and 25), with the following values of the parameters:  $M_{*,0,0} = 10.78$ ,  $M_{*,0,a} = 0.36$ ,  $M_{*,0,a^2} = 0$ ,  $M_{1,0} = 12.40$ ,  $M_{1,a} = 0.38$ ,  $\beta_0 = 0.45$ ,  $\beta_a = 0.026$ ,  $\delta_0 = 0.56$ ,  $\delta_a = 0$ ,  $\gamma_0 = 0.82$ ,  $\gamma_a = 1.86$ . The L12 fit for

<sup>2</sup> These values have been corrected by the authors after publication of W11.

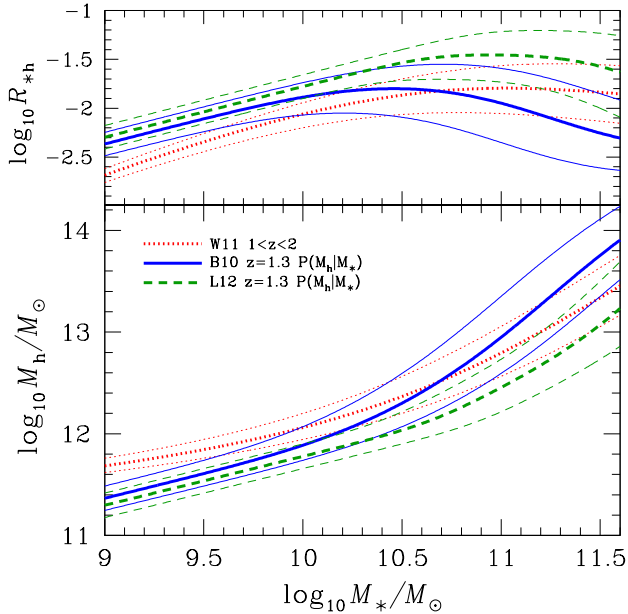


**Figure 4.** Stellar to DM mass ratio  $\mathcal{R}_{*h}$  (upper panel) and halo mass  $M_h$  (lower panel) as functions of stellar mass  $M_*$  according to prescriptions (i) (W11, thick solid lines), (ii) (B10, thick dotted lines) and (iii) (L12, thick dashed lines) for  $dM_*/dM_h$ . The corresponding thin lines show the estimated systematic uncertainty. In prescriptions (ii) and (iii) the SHMR depends on  $z$ : here we plot the fits for  $z = 1.3$  based on  $P(M_h|M_*)$ , which are described in Section 3.2.2.

$z = 1.3$  is also represented in Fig. 3 with the associated systematic uncertainty (0.25 dex in  $M_*$  at given  $M_h$ ).

### 3.2.2 Assigning dark-matter mass to galaxies: $M_h(M_*)$

In Section 3.2.1 we provided prescriptions to assign stellar mass to halos: for this purpose, we needed to compute the average stellar mass at given halo mass using the probability distribution  $P(M_*|M_h)$ . In order to build the initial conditions of our models we will also need to solve the inverse problem of assigning DM mass to observed galaxies of given stellar mass. This case is the topic of this Section.

Here the relevant probability distribution is  $P(M_h|M_*)$ . In prescriptions (ii) and (iii) of Section 3.2.1, the relation between  $M_*$  and  $M_h$  is explicitly obtained from  $P(M_*|M_h)$ .  $P(M_h|M_*)$  is related to  $P(M_*|M_h)$  by

$$P(M_h|M_*) = \frac{P(M_*|M_h)P(M_h)}{P(M_*)}, \quad (20)$$

where  $P(M_h)$  and  $P(M_*)$  are the stellar and halo mass functions. The average logarithmic halo mass at given stellar mass is then

$$\langle \log M_h \rangle (M_*) = \frac{\int P(M_*|M_h)P(M_h) \log M_h dM_h}{\int P(M_*|M_h)P(M_h) dM_h}, \quad (21)$$

independent of  $P(M_*)$  (see, e.g., appendix in Leauthaud et al. 2010). We compute  $\langle \log M_h \rangle (M_*)$  by numerically integrating the above equation, taking  $P(M_h)$  from Tinker et al. (2008, consistently with B10 and L12) and  $P(M_*|M_h)$  lognormal with logarithmic mean  $\langle \log M_* \rangle (M_h)$ , given by

prescriptions (ii) and (iii) in Section 3.2.1, and variance  $\sigma_{\log M_*}^2(z)$  (dependent on redshift, independent of  $M_h$ ). In both prescriptions (ii) and (iii) we adopt

$$\sigma_{\log M_*}(z) = \sqrt{x^2 + s^2(z)}, \quad (22)$$

where  $s(z) = s_0 + s_z z$ , with  $x = 0.16$ ,  $s_0 = 0.07$  and  $s_z = 0.05$  (see B10). The derived average value of  $\log M_h$  as a function of  $\log M_*$  is plotted in Fig. 4 (lower panel) at the reference redshift  $z = 1.3$ , for both prescription (ii) (B10) and prescription (iii) (L12) with the expected systematic uncertainty (0.25 dex in  $\log M_*$ ). In the case of the simpler prescription (i) we just invert equation (18) to obtain the value of  $\log M_h$  associated to a given value of  $\log M_*$  (dotted curves in Fig. 4). We note that the predicted values of  $\mathcal{R}_{*h}$  (upper panel of Fig. 4) for the relevant stellar masses  $\sim 10^{11} M_\odot$  are in the range  $-1.5 \lesssim \log \mathcal{R}_{*h} \lesssim -2$ . These numbers are broadly consistent within the error bars with a higher-redshift extrapolation of the independent estimate by Lagattuta et al. (2010), based on gravitational lensing.

As shown in Figs. 3 and 4, the SHMRs of the three considered prescriptions differ at  $z \sim 1.3$  in both shape and normalization. In addition, the SHMR evolves differently with redshift in prescriptions (ii) and (iii), while is independent of redshift in prescription (i). It follows that the stellar mass growth rate of the same galaxy is different in the three models, not only because different halo masses are assigned to the same descendant galaxy, but also because different stellar masses are assigned to satellite halos of a given mass. Though other choices of SHMRs would also be possible, we limit here to the three prescriptions described above, because they should give a sufficient measure of the effect of the current uncertainty on the SHMR. For instance, the SHMR obtained by Moster et al. (2010) lies in between L12 and B10 at low redshift (see figure 10 in L12). We verified that, within the uncertainties, this is the case also at higher  $z$ , at least up to the highest redshifts relevant to the present investigation ( $z \sim 2.2$ ).

### 3.3 Dry-merger driven evolution of $\sigma_0$ and $R_e$ ( $d\sigma_0/dM_*$ and $dR_e/dM_*$ )

The final ingredient for our model is the relation between evolution in stellar mass and that in velocity dispersion and effective radius, under the assumption of purely dissipationless mergers between spheroids. The evolution of the observable quantities  $\sigma_0$  and  $R_e$  is expected to depend non-trivially on the properties of the merger history, and in particular on the mass ratio  $\xi$  and orbital parameters of the mergers (for instance, orbital energy  $E$  and modulus of the orbital angular momentum  $L$ ). In general, we can write

$$\frac{d\sigma_0}{dM_*} = \frac{d\sigma_0}{dM_*}(\xi, E, L) \quad \text{and} \quad \frac{dR_e}{dM_*} = \frac{dR_e}{dM_*}(\xi, E, L). \quad (23)$$

In principle, these expressions can be estimated using  $N$ -body simulations of hierarchies of dissipationless mergers (e.g. Nipoti, Londrillo, & Ciotti 2003; Boylan-Kolchin, Ma, & Quataert 2006; N09b). However the parameter space  $\xi - E - L$  is prohibitively large and it has not been extensively explored so far. As a first-order approximation, we simplify the treatment by neglecting the dependence on  $E$  and  $L$ , so that we have

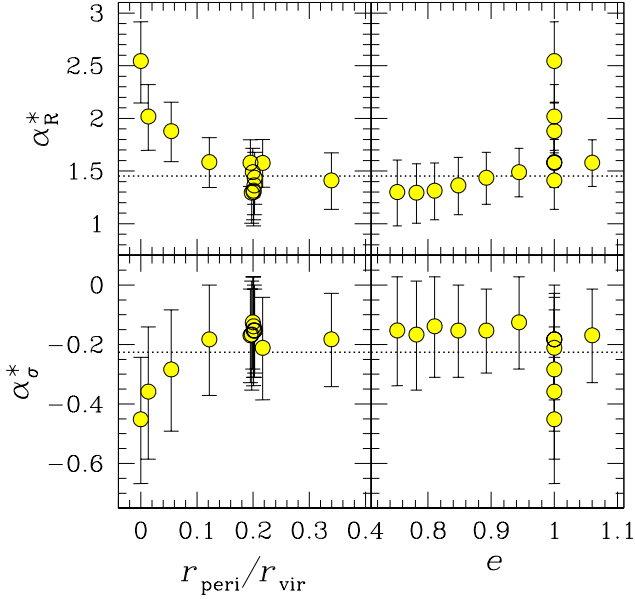


**Figure 5.** Distribution of slopes  $\alpha_\sigma^*$  and  $\alpha_R^*$  as functions of pericentric radius (left panels) and eccentricity (right panels) for our set of minor-merger simulations with mass ratio  $\xi = 0.2$  and  $\beta_R \simeq 0.6$  (see Section 3.3). The vertical bars indicate  $1\text{-}\sigma$  scatter due to projection effects. The dotted horizontal lines indicate the analytic estimates ( $\alpha_\sigma^* = f_\sigma$  and  $\alpha_R^* = f_R$ ) based on equations (28-29).

$$\frac{d\sigma_0}{dM_*} = \frac{d\sigma_0}{dM_*}(\xi) \quad \text{and} \quad \frac{dR_e}{dM_*} = \frac{dR_e}{dM_*}(\xi). \quad (24)$$

In the present work we will approximate the quantities  $d\sigma_0/dM_*(\xi)$  and  $dR_e/dM_*(\xi)$  with the analytic formulae described in Section 3.3.1, which are supported by the results of  $N$ -body simulations presented in Section 3.3.2.

### 3.3.1 Analytic estimates

In the simple case of parabolic orbit and negligible mass loss, the evolution of the virial velocity dispersion  $\sigma_v$  in a merger with mass ratio  $\xi$  can be written (see Naab, Johansson, & Ostriker 2009; Oser et al. 2012) as

$$f_\sigma \equiv \frac{d \ln \sigma_v}{d \ln M_*} = -\frac{1}{2} \left[ 1 - \frac{\ln(1 + \xi\epsilon)}{\ln(1 + \xi)} \right], \quad (25)$$

while the gravitational radius  $r_g$  evolves according to

$$f_R \equiv \frac{d \ln r_g}{d \ln M_*} = 2 - \frac{\ln(1 + \xi\epsilon)}{\ln(1 + \xi)}. \quad (26)$$

We defined  $\epsilon \equiv \sigma_{v,a}^2/\sigma_v^2$ , where  $\sigma_{v,a}$  is the virial velocity dispersion of the accreted system of mass  $\xi M_*$ . Note that the quantities  $\sigma_v$  and  $r_g$  refer to the total (DM plus stars) distribution of the galaxy, so the above expressions are strictly valid for two-component systems only if  $M_* \propto M_h$ . By assuming also a size-mass relation  $r_g \propto M_*^{\beta_R}$ , we can write

$$\epsilon = \xi^{1-\beta_R}, \quad (27)$$

so that, for fixed  $\beta_R$ , we obtain

$$f_\sigma(\xi) = -\frac{1}{2} \left[ 1 - \frac{\ln(1 + \xi^{2-\beta_R})}{\ln(1 + \xi)} \right], \quad (28)$$

and

$$f_R(\xi) = 2 - \frac{\ln(1 + \xi^{2-\beta_R})}{\ln(1 + \xi)} \quad (29)$$

(see also N12).

Assuming for simplicity  $\sigma_0 \propto \sigma_v$  and  $R_e \propto r_g$ , we obtain

$$\frac{d\sigma_0}{dM_*}(\xi) = \frac{\sigma_0}{M_*} f_\sigma(\xi), \quad \text{so } \sigma_0 \propto M_*^{f_\sigma(\xi)} \quad (30)$$

and

$$\frac{dR_e}{dM_*}(\xi) = \frac{R_e}{M_*} f_R(\xi), \quad \text{so } R_e \propto M_*^{f_R(\xi)}. \quad (31)$$

This approach takes into account in detail the dependence on the merging mass ratio, but assumes only parabolic orbits and neglects mass-loss and structural and dynamical non-homology (because  $\sigma_0$  and  $R_e$  are assumed proportional to the virial radius and gravitational radius of the total mass distribution). In order to model these additional complexities it is necessary to introduce complementary information based on  $N$ -body simulations.

### 3.3.2 $N$ -body simulations

We describe here the sets of  $N$ -body simulations of dissipationless galaxy mergers (in which the stars and DM are treated as distinguished components) that we use to support the analytic estimates introduced in the previous Section. The results of the  $N$ -body experiments can be parametrized by power-law relations between  $\sigma_0$  (or  $R_e$ ) and  $M_*$ . We expect that a family of merging hierarchies can be described by  $\sigma_0 \propto M_*^{\alpha_\sigma^*}$ , where  $\alpha_\sigma^*$  is characterized by a distribution with mean value  $\langle \alpha_\sigma^* \rangle$  and standard deviation  $\delta \alpha_\sigma^*$ , accounting for the diversity of merging histories and the range in mass ratios and orbital parameters (Boylan-Kolchin, Ma, & Quataert 2006; N09b). Similarly we expect<sup>3</sup>  $R_e \propto M_*^{\alpha_R^*}$ , with  $\alpha_R^*$  distributed with mean value  $\langle \alpha_R^* \rangle$  and standard deviation  $\delta \alpha_R^*$ . Numerical explorations allow us to evaluate how much the average virial expectation is affected by non-homology effects, and also to estimate the scatter around the average relations. N09b ran simulations of both major and minor mergers of spheroids, exploring extensively the parameter space only for major mergers. Therefore we adopt here the results for major mergers from N09b, and we supplement them with a new set of minor-merger simulations (see also Nipoti 2011).

The major-mergers hierarchies of N09b (a total of 22 equal-mass mergers, differing in orbital energy, angular momentum and dark-to-luminous mass ratio of the progenitors) are characterized by  $\langle \alpha_\sigma^* \rangle = 0.084$ ,  $\delta \alpha_\sigma^* = 0.081$  and  $\langle \alpha_R^* \rangle = 1.00$ ,  $\delta \alpha_R^* = 0.18$ , which we adopt as our fiducial values for  $\xi \sim 1$  mergers. The average values of these distributions are consistent with the predictions of equations (28-29), which in the case of major mergers give  $\alpha_R^* = f_R(1) = 1$  and  $\alpha_\sigma^* = f_\sigma(1) = 0$ , even though the simulations tend to

<sup>3</sup> The quantity  $\alpha_R^*$ , which measures the merging-induced variation in  $\log R_e$  for given variation in  $\log M_*$ , must not be confused with  $\beta_R$ , which is the logarithmic slope of the observed size-mass relation of ETGs. Only if  $\alpha_R^* \simeq \beta_R$  (which in fact is not the case) the size-mass relation would be preserved by dry mergers (Nipoti, Londrillo, & Ciotti 2003).



suggest  $\langle \alpha_\sigma^* \rangle > 0$ , which is likely to be a consequence of mass loss (N09a; N09b). We note that most of the simulations in (N09a) have progenitors with dark-to-luminous mass ratio  $M_h/M_* = 10$  (model A in N09a), while only four have  $M_h/M_* = 49$  (model D in N09a), which is expected to be more realistic. However, we verified that virtually the same values of  $\alpha_R^*$  and  $\alpha_\sigma^*$  reported above are found for either subsample.

In order to estimate the effects of non-homology and of the range of orbital parameters in the case of minor mergers, we ran a new set of 13  $N$ -body dissipationless simulations. In these simulations we model the encounter between a spherical galaxy with stellar mass  $M_*$  and DM mass  $10M_*$  (specifically, model A in N09a), and a galaxy with the same stellar and DM distributions and with stellar mass  $0.2M_*$  and DM mass  $2M_*$ . The size of the less massive galaxy is 0.36 of that of the main galaxy, so that the two galaxies lie on the size-stellar mass relationship  $R_e \propto r_g \propto M_*^{\beta_R}$  with  $\beta_R \simeq 0.6$ . The simulations were performed with the parallel  $N$ -body code FVFPS (Fortran Version of a Fast Poisson Solver; Londrillo, Nipoti, & Ciotti 2003; Nipoti, Londrillo, & Ciotti 2003), based on the Dehnen (2002) scheme. In the simulations the more massive galaxy is setup as an equilibrium two-component system with  $N_* \simeq 2 \times 10^5$  stellar particles and  $N_h \simeq 10^6$  DM particles, while the satellite has  $N_* \simeq 4 \times 10^4$  and  $N_h \simeq 2 \times 10^5$  (DM particles are twice as massive as stellar particles). We verified that these systems do not evolve significantly when simulated in isolation. In each merging simulation, at the initial time the distance between the centres of mass of the two systems equals the sum of their virial radii. The simulations differ in the initial relative velocity between the two systems, i.e. in the values of the orbital parameters: here we use eccentricity  $e$  and pericentric radius  $r_{\text{peri}}$  calculated in the point-mass approximation (see table in Nipoti 2011). Considering the entire set of 13 simulations,  $e$  is distributed with  $\langle e \rangle \simeq 0.93$  and  $\delta e \simeq 0.10$ , while  $r_{\text{peri}}$  (in units of the main-halo virial radius  $r_{\text{vir}}$ ) is distributed with  $\langle r_{\text{peri}}/r_{\text{vir}} \rangle \simeq 0.17$  and  $\delta(r_{\text{peri}}/r_{\text{vir}}) \simeq 0.09$  (for bound orbits only the circularity  $\eta$  is distributed with  $\langle \eta \rangle \simeq 0.53$  and  $\delta \eta \simeq 0.12$ ). These distributions compare favourably with those found in cosmological  $N$ -body simulations. For instance, there is good overlap between our distributions of parameters and those found for halo mergers (Benson 2005; Wang et al. 2005; Zentner et al. 2005; Khochfar & Burkert 2006; Wetzel 2011), though we are somewhat biased towards less bound orbits (for instance as compared to Wetzel 2011). However, the *scatter* in the orbital parameters of our simulations is comparable to that found by Wetzel (2011).

The 13 minor-merger simulations are followed up to virialization and the structural and kinematic properties of the remnants (defined selecting only bound particles) are measured as described in N09a. The values of  $\alpha_R^*$  and  $\alpha_\sigma^*$  for these 13 simulations are plotted in Fig. 5 as functions of  $e$  and  $r_{\text{peri}}/r_{\text{vir}}$ : overall, we obtain  $\langle \alpha_\sigma^* \rangle = -0.21$ ,  $\delta \alpha_\sigma^* = 0.097$  and  $\langle \alpha_R^* \rangle = 1.60$ ,  $\delta \alpha_R^* = 0.36$ . The horizontal lines show the predictions of equations (28-29) for  $\xi = 0.2$  and  $\beta_R \simeq 0.6$ , which are generally consistent with the average values found in the simulations (with the exceptions of accretions on very radial orbits, i.e. small  $r_{\text{peri}}$ ). We note that in the 13 minor-merging simulations we used models with relatively low dark-to-luminous mass ratio ( $M_h/M_* = 10$ ; model A

in N09a). To assess the dependence of our results on the value of  $M_h/M_*$ , we reran two of these simulations with the same orbital parameters ( $e = 1$ ,  $r_{\text{peri}} = 0$  and  $e = 1$ ,  $r_{\text{peri}}/r_{\text{vir}} \simeq 0.2$ ), but using galaxy models with  $M_h/M_* = 49$  (model D in N09a). In these cases we used  $N_* \simeq 10^5$  and  $N_h \simeq 2.5 \times 10^6$  for the main galaxy, and  $N_* \simeq 2 \times 10^4$  and  $N_h \simeq 5 \times 10^5$  for the satellite. We found that the higher- and lower- $M_h/M_*$  models lead to similar values of  $\alpha_\sigma^*$  and  $\alpha_R^*$ , with differences on the angle-averaged values always smaller than the scatter due to projection effects.

The fact that the numerical values of  $\langle \alpha_R^* \rangle$  and  $\langle \alpha_\sigma^* \rangle$  for both  $\xi = 1$  and  $\xi = 0.2$  are in good agreement with the virial predictions (28-29) suggests that we can use equations (30-31) to describe the *average* evolution of central velocity dispersion and effective radius (see also Oser et al. 2012). Our numerical study also finds significant scatter in  $\alpha_\sigma^*$  and in  $\alpha_R^*$ , due to projection effects (vertical bars in Fig. 5) and on the range of orbital parameters. This scatter must be taken into account when considering the dry-merger driven evolution of the scaling relations of ETGs (N09a; N09b; Nipoti 2011, see also Section 5.2).

### 3.4 Putting it all together

In this Section we describe how to combine the ingredients discussed in the previous Sections to answer the following question. Given a galaxy of a certain stellar mass  $M_*$ , size, and stellar velocity dispersion at  $z_d$  what did the progenitor at a higher  $z$  look like? In the following the progenitor is defined as the galaxy living in the most massive of the progenitor halos that by  $z_d$  have merged into the halo of our galaxy.

The first step is to assign a halo mass to a descendant galaxy observed at redshift  $z_d$ : once a SHMR is assumed, the halo mass is obtained univocally from the measured stellar mass using equation (21). Then, for a given halo mass at  $z_d$ , the evolution of the observable quantities can be obtained as follows. The growth in stellar mass can be written as

$$\frac{d^2 M_*}{dz d\xi} = \mathcal{R}_{*h}(\xi M_h, z) \xi M_h \frac{d^2 N_{\text{merg}}}{dz d\xi}(z, \xi, M_h), \quad (32)$$

where  $M_h = M_h(z)$  is the total mass of the halo (equation 5). By integrating over  $\xi$  we obtain

$$dM_* = -AI_M(z) M_h(z) \left[ \frac{M_h(z)}{10^{12} M_\odot} \right]^\alpha (1+z)^{\eta'} dz, \quad (33)$$

where

$$I_M(z) \equiv \int_{\xi_{\text{min}}}^1 \mathcal{R}_{*h}(\xi M_h, z) \xi^{\beta+1} \exp\left(\frac{\xi}{\xi}\right)^\gamma d\xi. \quad (34)$$

By integrating over  $z$  we obtain

$$M_*(z) = M_*(z_d) - AI_{\alpha, M}(z), \quad (35)$$

where

$$I_{\alpha, M}(z) \equiv \int_{z_d}^z I_M(z') \left[ \frac{M_h(z')}{10^{12} M_\odot} \right]^\alpha (1+z')^{\eta'} dz'. \quad (36)$$

The evolution of central velocity dispersion is given by

$$\frac{d^2 \ln \sigma_0}{dz d\xi} = f_\sigma(\xi) \mathcal{R}_{*h}(\xi M_h, z) \frac{M_h}{M_*} \xi \frac{d^2 N_{\text{merg}}}{dz d\xi}(z, \xi, M_h), \quad (37)$$

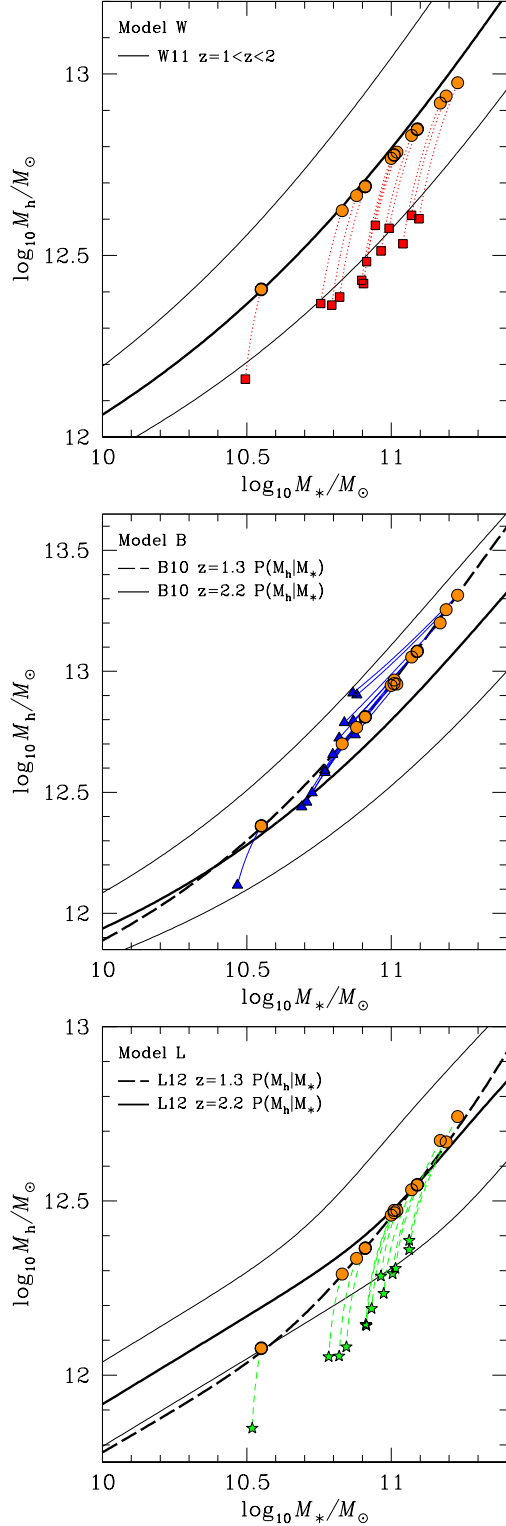


**Figure 6.** Location of the  $z \sim 1.3$  galaxies (circles; sample V1) and of the predicted  $z = 2.2$  progenitors (squares, triangles and stars) in the stellar mass-halo mass plane for model W (top panel), model B (intermediate panel) and model L (bottom panel). For comparison we also plot with thick lines the  $z = 1.3$  and  $z = 2.2$  fits of B10 and L12, and the (redshift-independent) fit by W11. Thin solid lines indicate the statistical scatter  $\sigma_{\log M_*}$  of the SHMR: in all cases we assume  $\sigma_{\log M_*}$  as given by equation (22), fixing  $z = 2.2$ .

where  $M_h = M_h(z)$  is calculated from equation (5) and  $M_* = M_*(z)$  is calculated from equation (35). By using equation (9) and integrating over  $\xi$  we obtain

$$d \ln \sigma_0 = -A I_\sigma(z) \frac{M_h(z)}{M_*(z)} \left[ \frac{M_h(z)}{10^{12} M_\odot} \right]^\alpha (1+z)^{\eta'} dz, \quad (38)$$

where

$$I_\sigma(z) \equiv \int_{\xi_{\min}}^1 f_\sigma(\xi) \mathcal{R}_{*h}(\xi M_h, z) \xi^{\beta+1} \exp\left(\frac{\xi}{z}\right)^\gamma d\xi. \quad (39)$$

Finally, by integrating over  $z$  we get

$$\ln \frac{\sigma_0(z)}{\sigma_0(z_d)} = -A I_{\alpha,\sigma}(z), \quad (40)$$

where

$$I_{\alpha,\sigma}(z) \equiv \int_{z_d}^z I_\sigma(z') \left[ \frac{M_h(z')}{10^{12} M_\odot} \right]^\alpha (1+z')^{\eta'} dz'. \quad (41)$$

Similar equations for the evolution of  $R_e$  can be obtained by replacing  $\sigma_0$  with  $R_e$ , and the subscript  $\sigma$  with the subscript  $R$  in equations (37-41).

#### 4 MODEL PREDICTIONS: HIGH-REDSHIFT PROGENITORS

We now turn to building specific realizations of our dry-merger evolution models and comparing them to observational data sets. To explore model uncertainties, we first computed models for the following range of parameters and prescriptions: minimum merger mass ratio between  $\xi_{\min} = 0.01$  and  $\xi_{\min} = 0.05$ ; prescription for  $dM_*/dM_h$  (i), (ii) or (iii); mass-size slope  $\beta_R = 0.5 - 0.8$ . It turns out that the predicted evolution of size, velocity dispersion and stellar mass depends almost exclusively on the adopted prescription for  $dM_*/dM_h$ , while the other parameters have relatively little effect. Therefore we focus here on models with  $\xi_{\min} = 0.03$  (see Section 3.1.3) and  $\beta_R = 0.6$  (the average value of  $d \ln R_e / d \ln M_*$  found by N12, almost independent of redshift).

In order to illustrate the effects of the main uncertainty we show the results of three models using different prescriptions of  $dM_*/dM_h$ : prescription (i) for model W, prescription (ii) for model B, and prescription (iii) for model L (see Section 3.2). The choice of the model also affects how we assign halo masses to each of our  $z \sim 1.3$  observed galaxies. Within each model we use the corresponding prescription at the appropriate redshift. The rest of this Section is organized as follows. In Section 4.1 we describe the size, velocity-dispersion and mass evolution of individual galaxies, presenting results obtained taking as descendant  $z \sim 1.3$  galaxies with measures of  $\sigma_0$  (sample V1). In Section 4.2 we focus on the question of the global size evolution of ETGs at high- $z$ , taking as descendants the ETGs with no measures of  $\sigma_0$  (sample R1).

##### 4.1 Size, velocity-dispersion and mass evolution of individual galaxies

We consider here results obtained taking as reference sample V1, i.e. the ETGs at  $z \sim 1.3$  with measured  $\sigma_0$ . The results obtained for models W, B and L, applied to the 13

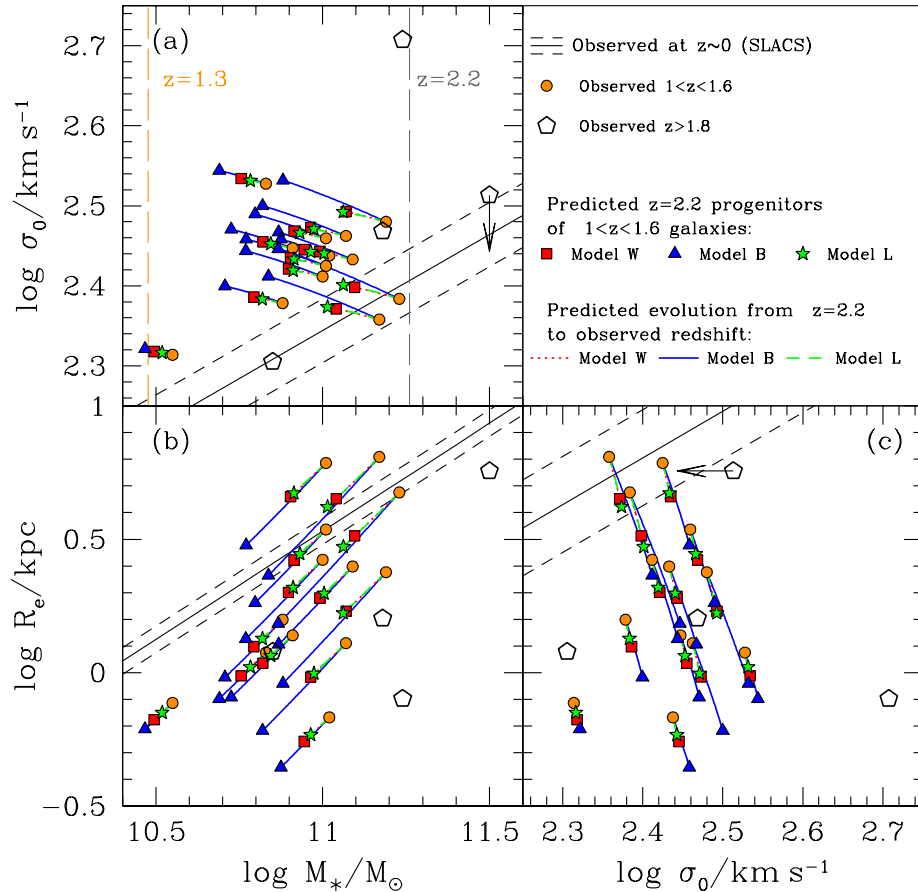


**Figure 7.** Distribution of observed ETGs and model galaxies in the stellar mass-velocity dispersion (panel a), stellar mass-effective radius (panel b), and velocity dispersion-effective radius (panel c) planes. The models trace the evolution of the ETGs of the  $1 < z < 1.6$  sample V1 (circles) from the observed redshift back to  $z = 2.2$  (triangles, squares and stars). Pentagons represent  $z > 1.8$  observed ETGs of sample V2. In panel a the vertical dashed lines indicate the minimum stellar mass necessary to measure velocity dispersion at  $z = 1.3$  and  $z = 2.2$  with current instruments. In each panel the solid line shows the corresponding scaling relation (with  $1\text{-}\sigma$  scatter; dashed lines) for the massive local ETGs of the SLACS sample Auger et al. (2010). The correlation between velocity dispersion and  $R_e$  (not reported in Auger et al. 2010) is  $\log R_e / \text{kpc} = (1.75 \pm 0.39) \log(\sigma_{e2}/200 \text{ km s}^{-1}) + 0.65 \pm 0.05$ , with intrinsic vertical scatter 0.18 in  $\log R_e$ . Here  $\sigma_{e2}$  is the velocity dispersion measured within  $R_e/2$ , which we assume to be related to  $\sigma_0$  (measured within  $R_e/8$ ) by  $\log \sigma_0 = \log \sigma_{e2} + 0.024$ .

descendants, are shown in Figs. 6-8. Given the small samples with measured  $\sigma_0$  available at moment, this exercise does not yield stringent constraints on dry-merger models (yet). Those will be derived in the next section with the aid of larger samples without measures of stellar velocity dispersion. However, our calculations illustrate the diagnostic power of large samples with measured stellar velocity dispersion, which are expected to be available soon. As an aid to forecast the outcome of future experiments, we provide simple fitting formulae that describe the predicted evolution of detailed properties of galaxies.

#### 4.1.1 Evolution in stellar mass and stellar-to-halo mass ratio

The 13 galaxies of sample V1 are assigned halo masses as described in Section 3.2.2. By considering three different SHMRs we can estimate systematic uncertainties in halo mass for given stellar mass, including those arising from un-

certainties in stellar mass estimates, which, for fixed IMF are of the order of 0.05 – 0.1 dex in the considered redshift range (Auger et al. 2009; Newman et al. 2012). The halo masses for the 13 galaxies of sample V1 at the observed redshift are in the range  $10^{12} \lesssim M_h/M_\odot \lesssim 2 \times 10^{13}$ . As expected from the curves shown in Fig. 4, halo masses tend to be higher in model B than in model L, while intermediate halo masses are predicted by model W. This is clearly seen in Fig. 6, where the reference galaxy models are plotted in the  $M_h$ - $M_*$  plane as filled circles. The stellar mass evolution predicted by the models can be also inferred from Fig. 7 (in  $M_*$ - $\sigma_0$  and  $M_*$ - $R_e$  planes; panels a and b), and Fig. 8 (in the redshift-stellar mass plane; bottom panel).

It is apparent that model B predicts stronger evolution in stellar mass than models W and L. The main reason for this difference is that the B10 SHMR at  $z \gtrsim 1$  is characterized by low values of  $\mathcal{R}_{*h} = M_*/M_h$  at  $M_* \gtrsim 10^{11} M_\odot$ , with  $\mathcal{R}_{*h}$  decreasing for increasing mass (Fig. 4). Therefore, in model B  $M_* \sim 10^{11} M_\odot$  galaxies are associated with quite

massive halos, for which the merger-driven mass-growth rate is found to be higher (Fakhouri, Ma, & Boylan-Kolchin 2010). In addition, these mergers are relatively star-rich, because of the shape of the SHMR at these high halo masses (Fig. 3), which implies that these systems systematically accrete lower-mass galaxies with higher baryon fraction. According to model B, stellar mass increases by factors between  $\sim 1.4$  (for the least massive galaxies) and  $\sim 2.3$  (for the most massive) in the time span between  $z \sim 2.2$  and  $z \sim 1.3$  (see Fig. 6, intermediate panel).

Models W and L predict significantly less evolution in stellar mass. In these cases the increase in  $M_*$  from  $z \sim 2.2$  to  $z \sim 1.3$  is between  $\sim 20\%$  for the least massive systems and  $\sim 50\%$  for the most massive (see Fig. 6, top and bottom panels). Even though the samples are small it is clear that the predicted progenitors tend to have lower  $M_*$  than the observed galaxies (see Figs. 7 and 8). However, the discrepancy can be at least partly ascribed to selection effects: galaxies with  $M_* \ll 10^{11} M_\odot$  at  $z \sim 2$  are too faint for a velocity dispersion measurement with current technology, while very massive galaxies might not be sampled by our lower redshift survey, either because they are very rare or because they have too low surface brightness.

A similar tension is observed between the predicted evolution of the dark-to-luminous mass ratio  $\mathcal{R}_{*h}$ , and that measured using abundance matching techniques. Although this comparison depends on the assumed SHMR, in general dry mergers tend to move galaxies away from the curves. The smaller deviation is observed for model B: in this case  $M_h$  is typically high compared with the SHMR, but the deviations are within the estimated scatter (Fig. 6, intermediate panel). For models W and L the model progenitors tend to deviate from the SHMR more than the related scatter (Fig. 6, top and bottom panels). Adding star formation to our models would not change the overall behaviour. In fact, star formation only makes  $\mathcal{R}_{*h}$  increase faster with redshift. Thus, the predicted positions of the progenitors in the  $M_*$ - $M_h$  plane (Fig. 6) would be shifted horizontally towards lower masses (thus reducing the deviation from the SHMR for models W and L, but increasing it for model B). Overall, the results shown in Fig. 6 indicate that the SHMR and its redshift evolution are critical constraints for dry-merging models. Given that  $\mathcal{R}_{*h}$  depends on mass, unequal mass dissipationless merging moves galaxies in a non trivial manner in the  $\mathcal{R}_{*h}$ - $M_h$  plane, in general away from the redshift dependent SHMR. A potential caveat is the SHMR is derived for all galaxies, not just ETGs. However, in the range of masses considered here the vast majority of central galaxies are indeed ETGs, and therefore this is not a concern.

#### 4.1.2 Evolution in velocity dispersion

A galaxy undergoing a dry merger with a lower velocity-dispersion system is expected to decrease its velocity dispersion (Nipoti, Londrillo, & Ciotti 2003; Naab, Johansson, & Ostriker 2009). For this reason our predicted  $z \sim 2.2$  progenitors tend to have higher  $\sigma_0$  than their  $z \sim 1.3$  descendants (see top panel in Fig. 8, and panels a and c in Fig. 7). However, the effect is small. In the case of models W and L the variation in  $\sigma_0$  is  $\lesssim 5\%$ . The more strongly evolving model B predicts variations up to  $\sim 15\%$ .

The combination of this weak change in  $\sigma_0$  and of the

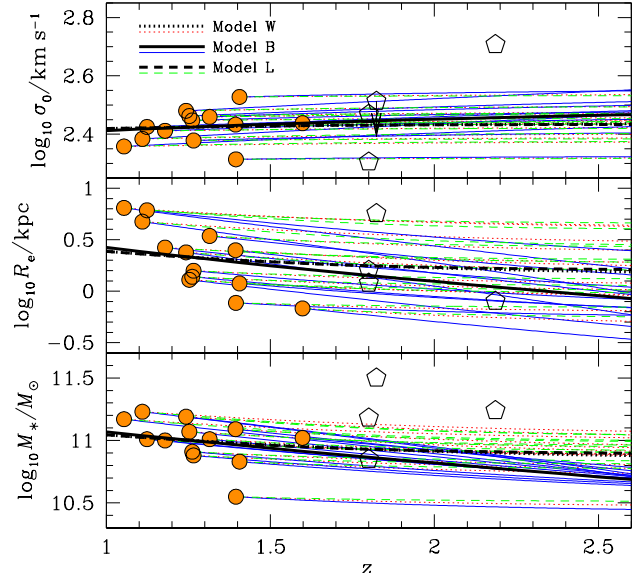


**Figure 8.** Predicted redshift evolution of central velocity dispersion  $\sigma_0$  (top panel), effective radius  $R_e$  (intermediate panel) and stellar mass  $M_*$  (bottom panel) for the ETGs of sample V1 (circles), according to the three different models (thin curves). The corresponding thick curves indicate the average values  $\langle \log \sigma_0 \rangle$ ,  $\langle \log R_e \rangle$  and  $\langle \log M_* \rangle$  as functions of  $z$ . Empty pentagons represent ETGs observed at  $z > 1.8$  (sample V2).

significant variation in stellar mass leads to predicted  $z \sim 2.2$  progenitors with substantially larger  $\sigma_0$  than local ETGs with similar stellar mass (Fig. 7, panel a). At the moment the reference sample of  $z \gtrsim 1.8$  ETGs with measured  $\sigma_0$  (sample V2) consists of only 4 galaxies. Three of them have  $M_* \gtrsim 1.5 \times 10^{11} M_\odot$  and cannot be dry-merging progenitors of our ETGs. The fourth galaxy (the least massive, with  $\log M_*/M_\odot = 10.85$ ) appears to lie on the local  $M_*$ - $\sigma_0$  relation, with lower  $\sigma_0$  than all our model progenitors. Lower mass galaxies are below the current limits.

We conclude by emphasizing that a strong prediction of the dry-merger model is that there should be a population of galaxies with high ( $\sim 300 \text{ km s}^{-1}$ ) stellar velocity dispersion and stellar mass in the range  $10.5 \lesssim \log M_*/M_\odot \lesssim 11$ . This prediction should be testable in the near future. In the short term, sensitive multiplexed near infrared spectrographs about to be commissioned on large telescopes (e.g. MOSFIRE on Keck; McLean et al. 2010) will be able to provide such samples at  $z > 1.5$ , where CaHK and the Gband region are redshifted into the Y and J bands. In the longer term, NIRSPEC on the James Webb Space Telescope will be able to extend velocity dispersion measurements to fainter galaxies and higher redshifts.

#### 4.1.3 Evolution in size

We discuss here the predicted evolution in size and in the size-mass relation for ETGs of sample V1. As expected, all models predict progenitors more compact than the descendants. Typically the relative variation in size is larger for more massive galaxies (see also Oser et al. 2010). As for

**Table 2.** Parameters of the linear best-fits of the correlations  $\langle \log M_*/M_\odot \rangle = a_M \log(1+z) + b_M$ ,  $\langle \log R_e/\text{kpc} \rangle = a_R \log(1+z) + b_R$  and  $\langle \log \sigma_0/\text{km s}^{-1} \rangle = a_\sigma \log(1+z) + b_\sigma$ .

Model	$a_M$	$b_M$	$a_R$	$b_R$	$a_\sigma$	$b_\sigma$
W	-0.67	11.23	-0.80	0.61	0.065	2.40
B	-1.48	11.52	-1.93	1.01	0.217	2.35
L	-0.60	11.21	-0.71	0.58	0.056	2.41

The fits represent the average evolution over the redshift interval  $1 \lesssim z \lesssim 2.5$  of the 13 ETGs of sample V1 (thick curves in Fig. 8), according to models W, B and L.

other observables, the size evolution is stronger in model B than in models W and L, (see panels b and c in Fig. 7, and intermediate panel in Fig. 8). Depending on the mass and redshift of the descendant, model B predicts an increase in  $R_e$  of a factor of 1.3 – 2.8 from  $z \sim 2.2$  to  $z \sim 1.3$ , while in the same redshift range models W and L predict at most a factor of  $\sim 1.6$  increase in  $R_e$ . Given the smallness and heterogeneity of our reference higher- $z$  sample V2, we cannot draw quantitative conclusion on the size evolution considering only galaxies with measured velocity dispersion. We defer the comparison of predicted and observed size evolution to Section 4.2, in which we will consider the larger samples R1 and R2.

#### 4.1.4 Describing the evolution of $M_*$ , $R_e$ and $\sigma$

In Fig. 8, together with the evolutionary tracks of the individual galaxies of sample V1, we plot also, as functions of redshift, the corresponding average quantities  $\langle \log M_* \rangle$ ,  $\langle \log R_e \rangle$  and  $\langle \log \sigma_0 \rangle$ . For convenience we provide linear fits to the average evolution in Table 2. These fits can be used to estimate the stellar-mass, size, and velocity-dispersion evolution predicted by our models for a typical massive ETG in the redshift range  $1 \lesssim z \lesssim 2.5$ . In particular, we parametrize the evolution of the three observables as  $M_* \propto (1+z)^{a_M}$ ,  $R_e \propto (1+z)^{a_R}$  and  $\sigma_0 \propto (1+z)^{a_\sigma}$ : considering the three models, the power-law indices lie in the following ranges:  $-1.5 \lesssim a_M \lesssim -0.6$ ,  $-1.9 \lesssim a_R \lesssim -0.7$  and  $0.06 \lesssim a_\sigma \lesssim 0.22$ . Combining the predicted mass and size evolution, we find that the effective stellar-mass surface density (which measures galaxy compactness) is predicted to evolve as  $M_*/R_e^2 \propto (1+z)^{0.8-2.4}$  in the redshift range  $1 \lesssim z \lesssim 2.5$ .

## 4.2 Global size evolution of early-type galaxies

In this section we apply our models to predict the progenitors of sample R1, i.e. 150 quiescent galaxies with  $1 \leq z \leq 1.6$ .

Figure 9 shows the progenitors of sample R1 in the  $M_*$ - $R_e$  plane, together with the observed population of quiescent galaxies at  $2 \lesssim z \lesssim 2.6$  (sample R2). In the same diagram we show the best-fit to the sample R2 data  $\log R_e/\text{kpc} = 0.14 + 0.59(\log M_*/M_\odot - 11)$ , with observed scatter  $\delta \log R_e = 0.23$  at given  $M_*$ . In all cases, the model progenitors populate mostly the region above the stellar mass-size relation, while there are no massive progenitors as compact as some very

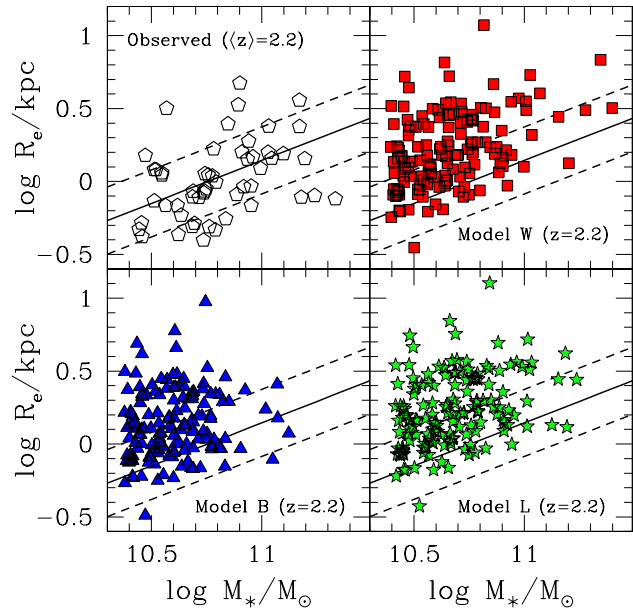


**Figure 9.** Distribution in the  $M_*$ - $R_e$  plane of galaxies observed at  $z > 2$  (empty pentagons; sample R2) and of  $z = 2.2$  progenitors predicted by our models for the 150 descendant quiescent galaxies at  $1 \leq z \leq 1.6$  (sample R1), for the three choices of SHMR (W,B,L). Symbols are the same as in Fig. 7. In each panel the solid line indicates the best-fit to the observed  $z > 2$  data, while the dashed lines indicate the associated observed scatter.

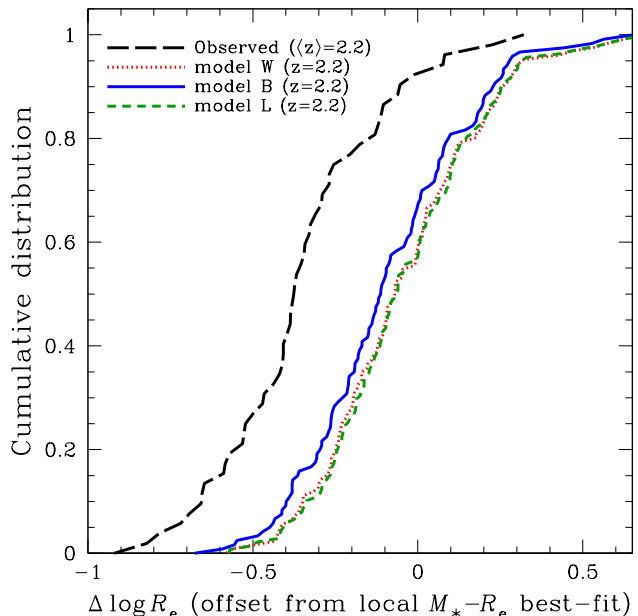


**Figure 10.** Cumulative distributions of the offset in  $\log R_e$  from local (SLACS; Auger et al. 2010)  $R_e$ - $M_*$  relationship for observed galaxies at  $z = 2 - 2.6$  (sample R2) and for  $z = 2.2$  progenitors predicted by models W, B and L for sample R1. For the models the distributions are computed considering only galaxies with  $M_* > 10^{10.45} M_\odot$  (i.e. adopting the same cut in stellar mass as for the observed sample).

dense ETGs observed at  $z \gtrsim 2$ . It is apparent that all models tend to predict progenitors with lower mass than the observed population at  $z \gtrsim 2$ . However, in all models there is a significant number of objects with stellar mass in the range  $10.45 \lesssim \log M_*/M_\odot \lesssim 11.5$  spanned by the observed ETGs.

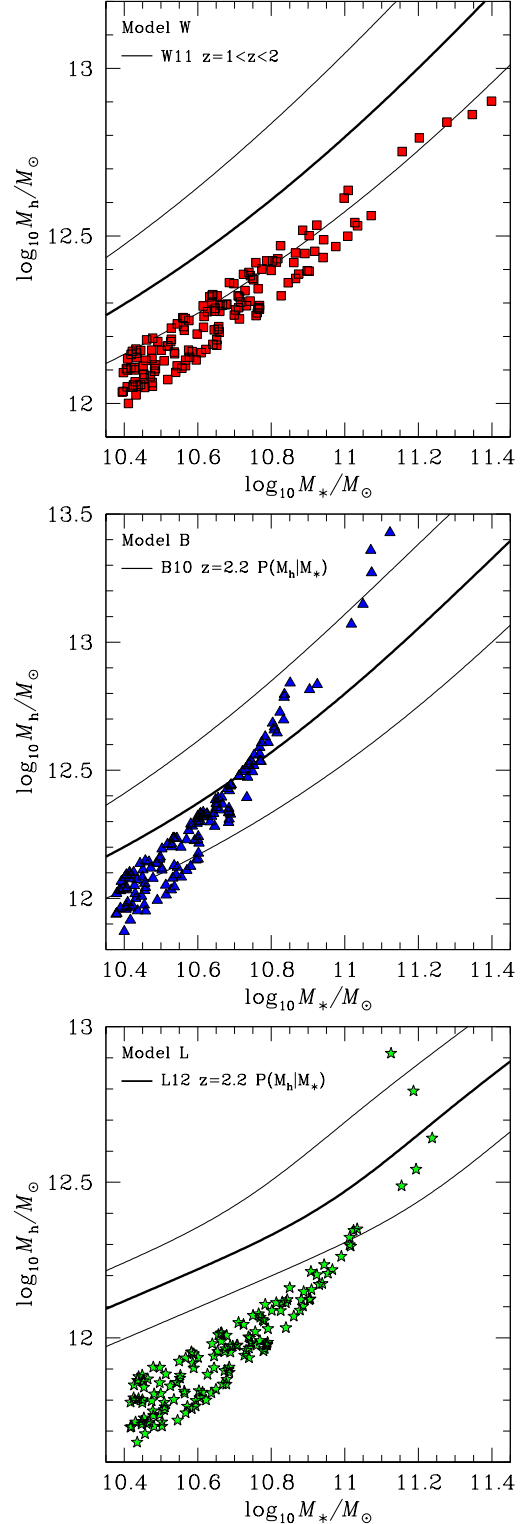
In order to quantify the difference between the predicted progenitors and the observed high- $z$  galaxies, we therefore select model progenitors with  $\log M_*/M_\odot \gtrsim 10.45$  and compute for each of them the vertical (i.e. in  $\log R_e$  at fixed  $M_*$ ) offset  $\Delta \log R_e$  with respect to the local (SLACS; Auger et al. 2010)  $M_*$ - $R_e$  correlation  $\log R_e/\text{kpc} = 0.81(\log M_*/M_\odot - 11) + 0.53$ . For comparison, we compute the same quantity for the ETGs observed at  $z \gtrsim 2$ . The parameter  $\Delta \log R_e$  is a normalized measure of compactness. By construction, normal (local) ETGs have  $\Delta \log R_e$  distributed around zero. Negative values of  $\Delta \log R_e$  indicate galaxies more compact than average. The cumulative distributions of the vertical offset  $\Delta \log R_e$ , shown in Fig. 10, clearly indicate that the predicted progenitors are more dense than local galaxies (median  $\Delta \log R_e \sim -0.1$ , i.e.  $R_e/R_{e,\text{local}} \sim 0.8$ ), but not as compact as observed ( $z \gtrsim 2$ ) galaxies (median  $\Delta \log R_e \sim -0.4$ , i.e.  $R_e/R_{e,\text{local}} \sim 0.4$ ). The progenitors tend to be more compact in model B than in model W and L, but definitely not enough to match the observed galaxies. In all cases, it is clear that the model progenitors and the observed galaxies do not belong to the same population (probability  $< 10^{-7}$  based on a Kolmogorov-Smirnov test).

Figure 11 illustrates the distribution of progenitors of sample R1 in the  $M_*$ - $M_h$  plane. This analysis confirms and strengthens the results of the analysis of the smaller sample V1 described in Section 4.1.1. The high- $z$  progenitors predicted by dry-merging models deviate substantially from the SHMR at the corresponding redshift. Only in model B the discrepancy is marginally consistent with the scatter of the SHMR.

Our findings suggest that a  $\Lambda$ CDM-based pure dry-merging model cannot explain the observation of ultra-compact massive quiescent galaxies at  $z \gtrsim 2$ . The discrepancy cannot be reduced by dissipative effects, which work in the opposite direction. Furthermore, even though the SHMR is quite uncertain at these redshifts, our results are robust and hold for all three SHMRs that we have tested here. The underlying physical reason is that in a pure dry-merging model fast evolution in size is necessarily associated with fast evolution in stellar mass. Therefore, if the progenitors of  $z \sim 1.3$  galaxies are forced to be as dense as the observed galaxies at  $z \sim 2.2$  they cannot be as massive.

## 5 CHECKING MODEL PREDICTIONS: LOW-REDSHIFT DESCENDANTS

The main focus of this paper is the evolution of ETGs in the relatively short time span ( $\sim 2$  Gyr) between  $z \sim 1.3$  and  $z \sim 2.2$ , in which most of the size evolution of ETGs appears to happen. We have demonstrated that  $\Lambda$ CDM-based dry-merger models have difficulties producing a fast enough size evolution in this redshift range. However it is important to perform a consistency check and compare our predictions with the milder size evolution observed between  $z \sim 1.3$  and  $z \sim 0$ . We consider only the evolution of sample V1,



**Figure 11.** Location of the predicted  $z = 2.2$  progenitors (squares, triangles and stars) in the stellar mass-halo mass plane for model W (top panel), model B (intermediate panel) and model L (bottom panel) of the 150 observed galaxies at  $1 < z < 1.6$  (sample R1). For comparison we also plot with thick lines the  $z = 2.2$  fits of B10 and L12, and the (redshift-independent) fit by W11. Thin solid lines indicate the statistical scatter  $\sigma_{\log M_*}$  of the SHMR: in all cases we assume  $\sigma_{\log M_*}$  as given by equation (22), fixing  $z = 2.2$ .

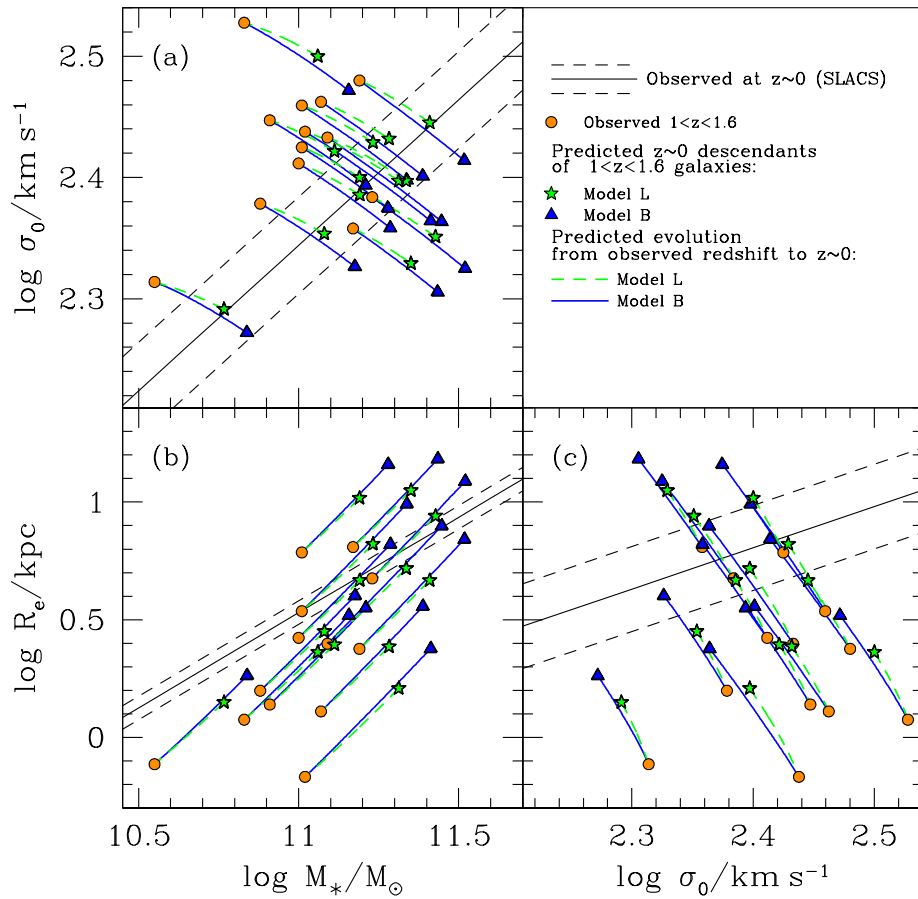


**Figure 12.** Same as Fig. 7, showing the future evolution of the  $z \sim 1.3$  ETGs (sample V1) to  $z = 0.19$  (the median redshift of the SLACS sample) for models L and B. The symbols are the same as in Fig. 7.

taking advantage of the diagnostic power of stellar velocity dispersion measurements.

In order to extend our models to  $z \sim 0$  we need the SHMR at  $z \lesssim 1$ . For this reason we restrict our analysis to models B and L, for which the SHMR is well measured in this redshift range (B10; L12, see Section 3.2.1). We leave all other model parameters unchanged. A potential concern is that the arguments used in Section 3.1.3 to constrain the value of  $\xi_{\min}$  between  $z \sim 2.2$  and  $z \sim 1.3$  do not necessarily apply to the longer time span between  $z \sim 1.3$  and  $z \sim 0$ . However, we verified empirically that the predicted evolution from  $z \sim 1.3$  to  $z \sim 0$  does not depend significantly on the specific choice of  $\xi_{\min}$ . In addition, we recall that we are assuming that our ETGs remain central halo galaxies as they evolve. While this is appropriate for massive galaxies at  $z > 1$ , at  $z \ll 1$  some of them might become satellite galaxies in clusters. However, this is a minor effect, since even in the local Universe the vast majority of massive galaxies ( $M_* \gtrsim 10^{11} M_\odot$ ) are believed to be central (see Section 3.1). We conclude that an extension of our models down to  $z \sim 0$  is sufficiently accurate for our purposes.

### 5.1 Predicted properties of $z \sim 0$ descendants

The location of the low-redshift model descendants of sample V1 in the  $M_*$ - $R_e$ - $\sigma_0$  space is shown in Fig. 12. For comparison, the observed local (SLACS) correlations are plotted in Fig. 12. For consistency, we have computed the evolution of model galaxies until  $z = 0.19$ , the median redshift of the SLACS sample (Auger et al. 2009).

The low-redshift descendants are found relatively close to the local observed correlation, albeit with considerable scatter (see Section 5.2). As for the higher redshift interval, model B predicts faster evolution than model L. In particular, we note that model B tends to “overshoot” the local  $M_*$ - $\sigma_0$  relationship, predicting massive descendants with velocity dispersion generally lower than that of observed local ETGs of similar mass, while the local descendants predicted by model L have  $\sigma$  consistent with observations (panel a in Fig. 12). In contrast, model B performs somewhat better than model L when compared with the local  $M_*$ - $R_e$  relation (panel b in Fig. 12), though in neither case the results are very satisfactory. This is shown quantitatively by Fig. 13, plotting the cumulative distributions of the vertical offset  $\Delta \log R_e$  from the local  $M_*$ - $R_e$  relation (introduced in Section 4.2) for the model  $z = 0.19$  descendants and for the observed SLACS galaxies. Not only the descendants tend to be, on average, too compact (the median offset is

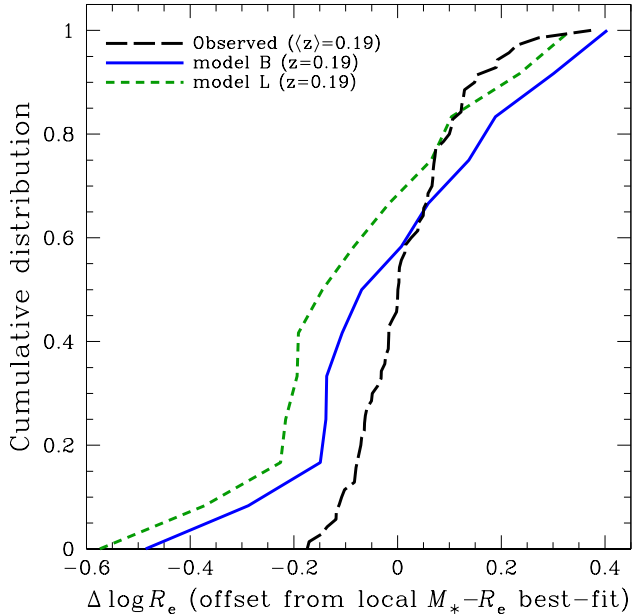


**Figure 13.** Same as Fig. 10, but for the  $z = 0.19$  predicted descendants of the  $z \sim 1.3$  ETGs (sample V1) for models L and B, and, for comparison, for the observed ETGs of the SLACS sample ( $\langle z \rangle = 0.19$ ; Auger et al. 2009).

$\Delta \log R_e \sim -0.07$  for model B and  $\Delta \log R_e \sim -0.15$  for model L), but also their distribution in the  $M_*$ - $R_e$  plane is characterized by quite large scatter (the predicted cumulative distributions are much shallower than the observed one; see Fig. 13). According to a Kolmogorov-Smirnov test, the probability that the model descendants and the observed galaxies belong to the same population is 0.1 for model B and 0.005 for model L.

It is also instructive to study the location of the descendants in the  $M_*$ - $M_h$  plane, shown in Fig. 14. The  $z = 0.19$  fit of the corresponding model is plotted for comparison, along with the  $z = 1.3$  fit. The  $z = 0.19$  descendants tend to have halo masses that are lower than those predicted by the corresponding SHMR. The most massive galaxies tend to deviate more from the SHMR, but in all cases the discrepancy is within the estimated scatter on the observationally determined SHMR (B10, L12). As discussed previously, star formation would make the discrepancy larger, which suggests that, within the context of a  $\Lambda$ CDM Universe, dissipative mergers cannot have contributed much to the growth of ETGs at  $z \lesssim 1$ .

We conclude that the relatively mild *average* evolution of ETGs between  $z \sim 1.3$  and  $z \sim 0$  is consistent with a  $\Lambda$ CDM-based dry-merger model. However, as we discuss in the next section, explaining the tightness of the local scaling relations is a much more formidable challenge.

## 5.2 Scatter in the scaling laws

It is well known that the local observed scaling relations of ETGs are remarkably tight. The existence of these scaling laws and their tightness represent a severe challenge for any theory of galaxy formation. For example, it has been shown that it is hard to bring ETGs onto the local scal-

ing laws (within their small scatter) via a stochastic growth process such as merging (Nipoti, Londrillo, & Ciotti 2003; Ciotti, Lanzoni, & Volonteri 2007; Nair, van den Bergh, & Abraham 2011, N09a; N09b). In this paper we have assumed that every ETG evolves according to the expected *average* growth history. In this way, we have so far neglected several sources of scatter in the properties of progenitor or descendant galaxies. In other words, two identical ETGs at a given redshift are predicted by our models to have identical progenitors and identical descendants. This is clearly not realistic, because we expect a distribution of merging histories. An additional source of scatter is the *intrinsic* scatter of the SHMR that we adopt to match stars and halos. Finally, the distribution of merger orbital parameters adds scatter to the distribution of the slopes  $\alpha_R^*$  and  $\alpha_\sigma^*$  characterizing the evolution of  $R_e$  and  $\sigma_0$  during an individual merger event (see Section 3.3).

These additional sources of scatter are clearly a problem. The size-mass-velocity dispersion correlations of our  $z \sim 0$  model descendants are already characterized by a substantial spread (see Figs. 12-13), even neglecting these effects. In part, the spread might reflect observational uncertainties in the data. However, this is a small effect. N12 recently showed that the observed scatter of the  $M_*$ - $R_e$  relation does not increase significantly with redshift in the range  $0.4 < z < 2.5$ . Therefore, unless there is some form of fine tuning or conspiracy, we expect that inclusion of the aforementioned sources of intrinsic scatter would lead to even larger spread.

Consider for example, the expected scatter in  $d\sigma/dM_*$  and  $dR_e/dM_*$  due to the range of merging orbital parameters. By combining the simulations of N09a with the set of minor-merging simulations presented in Section 3.3, we find that the tightness of the local  $M_*$ - $R_e$  implies that local massive ETGs can have assembled at most  $\sim 45\%$  of their stellar mass via dry mergers during their entire merger history. This is the upper limit, under extreme fine tuning (see Nipoti 2011, for details). For comparison, our cosmologically motivated models predict  $z \sim 0$  descendant ETGs to have assembled  $\sim 50 - 60\%$  (B) and  $\sim 40 - 50\%$  (L) of their stellar mass via dry merger *since*  $z = 1.3$  (see panels a and b in Fig. 12). This is higher than the maximum limit for extreme fine tuning. Taking into account the additional scatter in the SHMR and in the merging history would only exacerbate the problem. This result, based on cosmologically motivated merger histories, extends and supersedes that obtained by N09b under more idealized conditions.

## 6 DISCUSSION

We have developed dry-merging evolution models of ETGs based on cosmologically determined merger rates and calibrated on  $N$ -body simulations of individual mergers between spheroids. This hybrid strategy allowed us to compute accurately observables such as size, stellar velocity dispersion and mass, and their evolution within a cosmological context. Dissipative effects were neglected, so as to maximize the predicted decrease in density with time. This conservative approach allowed us to draw general conclusions on the ability of  $\Lambda$ CDM merging models to reproduce the observed size evolution.



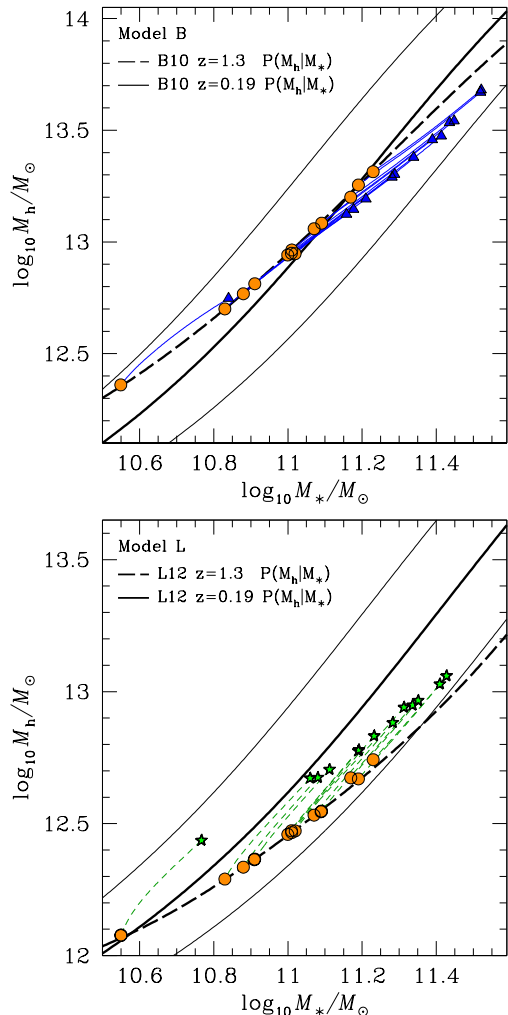


**Figure 14.** Same as Fig. 6, but showing the future evolution of the reference  $z \sim 1.3$  ETGs (sample V1) to  $z = 0.19$  for model B (upper panel) and model L (lower panel). The symbols are the same as in Fig. 7. Thin solid lines indicate the statistical scatter  $\sigma_{\log M_*}$  of the SHMR: for model B we take  $\sigma_{\log M_*}$  as given by equation (22) with  $z = 0.19$ ; for model L we assume  $\sigma_{\log M_*} = 0.2$  (see L12).

The predictions of our models were tested by considering two well defined samples of ETGs at  $z \sim 1.3$ , computing the predicted properties of their progenitors at  $z \sim 2.2$  and comparing them to those of real observed galaxies. As an additional check, we have tested our predictions against the local scaling laws of ETGs.

Our main finding is that the size evolution of massive ETGs from  $z \gtrsim 2$  to  $z \sim 1.3$  cannot be explained exclusively by dissipationless major and minor merging. This result is robust with respect to uncertainties in the correlation between stellar and halo mass at  $z \gtrsim 1$ . Intuitively and qualitatively, the main motivation is that size growth is coupled to mass growth even in minor mergers. Therefore, substantial size growth also requires significant mass growth, more than the evolution in the stellar mass function would allow. Furthermore, significant size growth requires several mergers and increased scatter in the scaling relations, larger than their tightness in the local universe would allow.

In addition to the evolution in stellar mass, size, and stellar velocity dispersion of ETGs, we studied the redshift evolution of their dark-to-luminous mass ratio under the same dry-merging scenario. A comparison of the predicted evolution with the measured one shows a similar tension between theory and data. Dry mergers tend to move galaxies away from the observed SHMRs, suggesting, e.g., that a pure dry-merging scenario is inconsistent with a redshift-independent SHMR at  $z \gtrsim 1$ . Even though more accurate measurements of the SHMR are needed to draw strong conclusions, it is clear that this is a promising observational diagnostic tool of dry-merger models.

One important caveat to our analysis is that we assume that the progenitors of local or intermediate redshift ETGs are also spheroids. Theoretically it is possible that they might be disk-dominated (see, e.g., Feldmann et al. 2010). Observationally, it is not clear whether this assumption is justified, since the morphology of high- $z$  massive compact galaxies is not always well determined and they might include a large fraction of disk-dominated systems (van der Wel et al. 2011; Weinzirl et al. 2011). Conversely, it is also possible that the present-day descendants of  $z \gtrsim 2$  ETGs might be disk galaxies (Graham 2011). The key question is how much are results changed if we allow for morphological transformations. A quantitative answer to this question would require numerical investigation beyond the scope of this paper. Qualitatively, the strict coupling between mass and size evolution ultimately comes from energy conservation. Therefore it should hold independently of the morphology of the merging galaxies.

Throughout the paper we have also assumed that during a merger the accreted system is a spheroidal galaxy lying on the observed size-mass relation of ETGs ( $R_e \propto M_*^{\beta_R}$  with  $\beta_R \sim 0.6$ ). In principle, it is possible that a substantial fraction of the accreted satellites are low-surface density disk galaxies, which do not form stars efficiently and deposit most of their stellar mass in the outskirts of the main galaxy. This might be a more efficient mechanism to increase galaxy size for given increase in stellar mass. *Ad hoc* numerical simulations would be required to assess the possible effect of this process quantitatively: to zero-th order approximation such an effect can be implemented in our model by forcing a value of  $\beta_R$  smaller than observed for ETGs which implies stronger size evolution (see equation 29). However, as pointed out above, it turns out that varying  $\beta_R$  has a relatively small effect on the predicted size evolution, which is not sufficient to reconcile the models with the observations.

Our findings suggest that the ultra-dense high- $z$  ETGs might be an anomaly even in a hierarchical  $\Lambda$ CDM universe in which most mergers are dry. In principle, this might be indicating that the actual dry-merger rate is higher than predicted by the considered  $\Lambda$ CDM model (for instance, because the cosmological parameters are substantially different from what we assume; see also Section 3.1.2). To test this hypothesis we can compare the merger rate of our models with the merger rate inferred from observations of galaxy pairs. For instance, N12, considering mergers with mass ratios  $> 0.1$ , find that in the redshift range  $1.5 < z < 2$  the typical merger rate per galaxy is  $dN_{\text{merg}}/dt = 0.18 \pm 0.06/\tau$  (for observed quiescent galaxies with  $M_* \gtrsim 10^{10.4} M_\odot$ ), where  $\tau = 1 - 2$  Gyr is the merging time. Adopting the same cut in stellar mass, merger mass ratio and redshift, we find, on

average,  $dN_{\text{merg}}/dt \simeq 0.22 \text{ Gyr}^{-1}$  (model W),  $dN_{\text{merg}}/dt \simeq 0.4 \text{ Gyr}^{-1}$  (model B) and  $dN_{\text{merg}}/dt \simeq 0.17 \text{ Gyr}^{-1}$  (model L), taking as descendant sample R1. This means that in fact the model merger rates tend to be higher than those estimated observationally, so it is unlikely that the difficulties of  $\Lambda$ CDM dry-merger models are due to an underestimate of the merger rate.

Alternatively, the tension between the data and the model might be alleviated if there are other physical processes, not included in our models, that contribute to make galaxies less compact with evolving cosmic time. An interesting proposal is expansion due to gas loss following feedback from AGN (Fan et al. 2008, 2010), which, in principle, could naturally explain the observation that most of the size evolution occurs at higher redshift, when AGN feedback is believed to be most effective. However, no satisfactory fully self-consistent model of size evolution via AGN feedback has been proposed so far and it is not clear whether it can be a viable solution. In particular, it appears hard to reconcile this scenario with the relatively old stellar populations of the observed compact high- $z$  ETGs, because the characteristic timescale of expansion due to AGN-driven mass loss is so short that the galaxy is expected to have already expanded when it appears quiescent (Ragone-Figueroa & Granato 2011). Otherwise, it is possible that observations are affected by systematics or selection biases which maybe not fully understood (Hopkins et al. 2010a; Mancini et al. 2010; Oser et al. 2012).

## 7 CONCLUSIONS

The goal of this paper was to investigate whether dry merging alone is sufficient to explain the observed size evolution of elliptical galaxies from  $z \gtrsim 2$  to the present. We focused primarily on the short  $\sim 1.8 \text{ Gyr}$  time span between  $z \sim 2.2$  and  $z \sim 1.3$  when much of the size evolution appears to take place. We find that the observed size evolution is in fact stronger than predicted by  $\Lambda$ CDM dry-merging models. Quantitatively, our main results can be summarized as follows:

(i) According to our  $\Lambda$ CDM-based pure dry-merging models, at redshifts  $1 \lesssim z \lesssim 2.5$  a typical massive ( $M_* \sim 10^{11} M_\odot$ ) ETG is expected to evolve in stellar mass as  $M_* \propto (1+z)^{a_M}$ , size as  $R_e \propto (1+z)^{a_R}$  and velocity dispersion as  $\sigma_0 \propto (1+z)^{a_\sigma}$ , with  $-1.5 \lesssim a_M \lesssim -0.6$ ,  $-1.9 \lesssim a_R \lesssim -0.7$  and  $0.06 \lesssim a_\sigma \lesssim 0.22$ ; the corresponding evolution in stellar-mass surface density is  $M_*/R_e^2 \propto (1+z)^{0.8-2.4}$ .

(ii) The predicted  $z \gtrsim 2$  dry-merger progenitors of  $z \sim 1.3$  massive ETGs are, on average, less massive and less compact than the real massive quiescent galaxies observed at similar redshifts. The median offset from the local  $M_*$ - $R_e$  relationship is  $\Delta \log R_e \sim -0.1 \text{ dex}$  (i.e.  $R_e/R_{e,\text{local}} \sim 0.8$ ) for model progenitors, and  $\Delta \log R_e \sim -0.4 \text{ dex}$  (i.e.  $R_e/R_{e,\text{local}} \sim 0.4$ ) for observed high- $z$  galaxies, i.e. the latter are smaller in size by a factor of  $\sim 2$  at given stellar mass.

(iii) Dry mergers introduce substantial scatter in the scaling relations of ETGs. Even models that reproduce the average size evolution from  $z \lesssim 1.3$  to  $z \sim 0$  require extreme fine tuning to be consistent with the small scatter of the local scaling laws. For instance, our  $\Lambda$ CDM-based models predict that local massive ETGs have accreted  $\sim 40 - 60\%$

of their stellar mass via dry mergers since  $z \sim 1.3$ . However, the tightness of the local  $R_e$ - $M_*$  relation implies that these ETGs can have accreted in this way at most  $\sim 45\%$  of their stellar mass over their *entire* assembly history (with extreme fine tuning; see also Nipoti 2011; Nipoti, Treu, & Bolton 2009a; Nipoti et al. 2009b).

Our conclusion is thus that dry mergers alone, whether minor or major, are *insufficient* to explain the observed growth of massive galaxies. This is in good agreement with the results of several studies, including that by N12 and those of Fan et al. (2010); Shankar et al. (2011). It is interesting to compare in particular with the results by N12, which are based on the same dataset, augmented by number density considerations, but a completely different analysis. N12 show that the observed number of merging satellites is insufficient to cause sufficient evolution, while we show that the theoretically predicted rates are insufficient. Given the completely different analysis and different systematic uncertainties it is encouraging that the results are mutually consistent.

## ACKNOWLEDGEMENTS

We are grateful to Peter Behroozi and Richard Ellis for insightful comments on an earlier version of this manuscript. We thank Michael Boylan-Kolchin and Carlo Giocoli for helpful discussions. We acknowledge the CINECA Awards N. HP10C2TBYB (2011) and HP10CQFATD (2011) for the availability of high performance computing resources. C.N. is supported by the MIUR grant PRIN2008, T.T. by the Packard Foundation through a Packard Research Fellowship. We also acknowledge support by World Premier International Research Center Initiative (WPI Initiative), MEXT, Japan.

## REFERENCES

- Angulo R. E., White S. D. M., 2010, MNRAS, 405, 143
- Auger M. W., Treu T., Bolton A. S., Gavazzi R., Koopmans L. V. E., Marshall P. J., Bundy K., Moustakas L. A., 2009, ApJ, 705, 1099
- Auger M. W., Treu T., Bolton A. S., Gavazzi R., Koopmans L. V. E., Marshall P. J., Moustakas L. A., Burles S., 2010, ApJ, 724, 511
- Behroozi P. S., Conroy C., Wechsler R. H., 2010, ApJ, 717, 379 (B10)
- Benson A. J., 2005, MNRAS, 358, 551
- Bernardi M., Roche N., Shankar F., Sheth R. K., 2011, MNRAS, 412, L6
- Bluck A. F. L., Conselice C. J., Buitrago F., Gruetzbauch R., Hoyos C., Mortlock A., Bauer A. E., 2011, arXiv, arXiv:1111.5662
- Boylan-Kolchin M., Ma C.-P., Quataert E., 2006, MNRAS, 369, 1081
- Boylan-Kolchin M., Ma C.-P., Quataert E., 2008, MNRAS, 383, 93
- Boylan-Kolchin M., Springel V., White S. D. M., Jenkins A., Lemson G., 2009, MNRAS, 398, 1150
- Cappellari M., et al., 2009, ApJ, 704, L34
- Cassata P., et al., 2011, ApJ, 743, 96

- Cenarro A. J., Trujillo I., 2009, *ApJ*, 696, L43  
 Chabrier G., 2003, *PASP*, 115, 763  
 Cimatti A., et al., 2008, *A&A*, 482, 21  
 Cimatti A., Nipoti C., Cassata P., 2011, in preparation  
 Ciotti L., Lanzoni B., Volonteri M., 2007, *ApJ*, 658, 65  
 Cooper M. C., et al., 2012, *MNRAS*, 419, 3018  
 Covington M. D., Primack J. R., Porter L. A., Croton D. J., Somerville R. S., Dekel A., 2011, *MNRAS*, 415, 3135  
 Daddi E., et al., 2005, *ApJ*, 626, 680  
 Dehnen W., 2002, *JCoPh*, 179, 27  
 Damjanov I., et al., 2011, *ApJ*, 739, L44  
 Fakhouri O., Ma C.-P., 2010, *MNRAS*, 401, 2245  
 Fakhouri O., Ma C.-P., Boylan-Kolchin M., 2010, *MNRAS*, 406, 2267  
 Fan L., Lapi A., De Zotti G., Danese L., 2008, *ApJ*, 689, L101  
 Fan L., Lapi A., Bressan A., Bernardi M., De Zotti G., Danese L., 2010, *ApJ*, 718, 1460  
 Feldmann R., Carollo C. M., Mayer L., Renzini A., Lake G., Quinn T., Stinson G. S., Yepes G., 2010, *ApJ*, 709, 218  
 Genel S., Bouché N., Naab T., Sternberg A., Genzel R., 2010, *ApJ*, 719, 229  
 Graham A. W., 2011, arXiv, arXiv:1108.0997  
 Guo Q., White S., Li C., Boylan-Kolchin M., 2010, *MNRAS*, 404, 1111  
 Hausman M. A., Ostriker J. P., 1978, *ApJ*, 224, 320  
 Hernquist L., Spergel D. N., Heyl J. S., 1993, *ApJ*, 416, 415  
 Hopkins P. F., Hernquist L., Cox T. J., Keres D., Wuyts S., 2009, *ApJ*, 691, 1424  
 Hopkins P. F., Bundy K., Hernquist L., Wuyts S., Cox T. J., 2010a, *MNRAS*, 401, 1099  
 Hopkins P. F., et al., 2010b, *ApJ*, 724, 915  
 Kereš D., Katz N., Weinberg D. H., Davé R., 2005, *MNRAS*, 363, 2  
 Khochfar S., Burkert A., 2006, *A&A*, 445, 403  
 Klypin A. A., Trujillo-Gomez S., Primack J., 2011, *ApJ*, 740, 102  
 Komatsu E., et al., 2011, *ApJS*, 192, 18  
 Kriek M., et al., 2008, *ApJ*, 677, 219  
 Lacey C., Cole S., 1993, *MNRAS*, 262, 627  
 Lagattuta D. J., et al., 2010, *ApJ*, 716, 1579  
 Leauthaud A., et al., 2010, *ApJ*, 709, 97  
 Leauthaud A., Tinker J., Behroozi P. S., Busha M. T., Wechsler R. H., 2011a, *ApJ*, 738, 45  
 Leauthaud A., et al., 2012, *ApJ*, 744, 159 (L12)  
 Londrillo P., Nipoti C., Ciotti L., 2003, in “Computational astrophysics in Italy: methods and tools”, Roberto Capuzzo-Dolcetta ed., Mem. S.A.It. Supplement, vol. 1, p. 18  
 Mancini C., et al., 2010, *MNRAS*, 401, 933  
 McLean I. S., et al., 2010, *SPIE*, 7735, 47  
 Moster B. P., Somerville R. S., Maulbetsch C., van den Bosch F. C., Macciò A. V., Naab T., Oser L., 2010, *ApJ*, 710, 903  
 Naab T., Johansson P. H., Ostriker J. P., 2009, *ApJ*, 699, L178  
 Nair P., van den Bergh S., Abraham R. G., 2011, *ApJ*, 734, L31  
 Newman A. B., Ellis R. S., Treu T., Bundy K., 2010, *ApJ*, 717, L103 (N10)  
 Newman A. B., Ellis R. S., Bundy K., Treu T., 2012, *ApJ*, in press, arXiv:1110.1637 (N12)  
 Nipoti C., Londrillo P., Ciotti L., 2003, *MNRAS*, 342, 501  
 Nipoti C., Treu T., Bolton A. S., 2009a, *ApJ*, 703, 1531 (N09a)  
 Nipoti C., Treu T., Auger M. W., Bolton A. S., 2009b, *ApJ*, 706, L86 (N09b)  
 Nipoti C., 2011, arXiv, arXiv:1109.1669  
 Onodera M., et al., 2010, *ApJ*, 715, L6  
 Oser L., Ostriker J. P., Naab T., Johansson P. H., Burkert A., 2010, *ApJ*, 725, 2312  
 Oser L., Naab T., Ostriker J. P., Johansson P. H., 2012, *ApJ*, 744, 63  
 Ragone-Figueroa C., Granato G. L., 2011, *MNRAS*, 414, 3690  
 Raichoor A., et al., 2012, *ApJ*, 745, 130  
 Robertson B., Cox T. J., Hernquist L., Franx M., Hopkins P. F., Martini P., Springel V., 2006, *ApJ*, 641, 21  
 Saracco P., Longhetti M., Andreon S., 2009, *MNRAS*, 392, 718  
 Saracco P., Longhetti M., Gargiulo A., 2011, *MNRAS*, 412, 2707  
 Shankar F., Marulli F., Bernardi M., Mei S., Meert A., Vikram V., 2011, arXiv, arXiv:1105.6043  
 Springel V., et al., 2005, *Natur*, 435, 629  
 Stiavelli M., et al., 1999, *A&A*, 343, L25  
 Tinker J., Kravtsov A. V., Klypin A., Abazajian K., Warren M., Yepes G., Gottlöber S., Holz D. E., 2008, *ApJ*, 688, 709  
 Trujillo I., et al., 2006, *ApJ*, 650, 18  
 van den Bosch F. C., et al., 2007, *MNRAS*, 376, 841  
 van den Bosch F. C., Aquino D., Yang X., Mo H. J., Pasquali A., McIntosh D. H., Weinmann S. M., Kang X., 2008, *MNRAS*, 387, 79  
 van der Wel A., Holden B. P., Zirm A. W., Franx M., Retura A., Illingworth G. D., Ford H. C., 2008, *ApJ*, 688, 48  
 van der Wel A., Bell E. F., van den Bosch F. C., Gallazzi A., Rix H.-W., 2009, *ApJ*, 698, 1232  
 van der Wel A., et al., 2011, *ApJ*, 730, 38  
 van de Sande J., et al., 2011, *ApJ*, 736, L9  
 van Dokkum P. G., et al., 2008, *ApJ*, 677, L5  
 van Dokkum P. G., Kriek M., Franx M., 2009, *Nature*, 460, 717  
 Wake D. A., et al., 2011, *ApJ*, 728, 46 (W11)  
 Wang H. Y., Jing Y. P., Mao S., Kang X., 2005, *MNRAS*, 364, 424  
 Weinzirl T., et al., 2011, *ApJ*, 743, 87  
 Wetzel A. R., Cohn J. D., White M., 2009, *MNRAS*, 395, 1376  
 Wetzel A. R., 2011, *MNRAS*, 412, 49  
 Zentner A. R., Berlind A. A., Bullock J. S., Kravtsov A. V., Wechsler R. H., 2005, *ApJ*, 624, 505  
 Zirm A. W., et al., 2007, *ApJ*, 656, 66